

12

SECURITY CLASSIFICATION OF THIS PAGE (When Data Entered)

REPORT DOCUMENTATION PAGE		READ INSTRUCTIONS BEFORE COMPLETING FORM
1. REPORT NUMBER	2. GOVT ACCESSION NO.	3. RECIPIENT'S CATALOG NUMBER
4. TITLE (and Subtitle) Application of Solidification Theory to Rapid Solidification Processing		5. TYPE OF REPORT & PERIOD COVERED Semi-annual technical report Oct. 1, 1983 to March 31, 1984
		5. PERFORMING ORG. REPORT NUMBER
7. AUTHOR(s) W. J. Boettinger, J. W. Cahn, S. R. Coriell, J. R. Manning and R. J. Schaefer		5. CONTRACT OR GRANT NUMBER(s) ARPA Order 3751
5. PERFORMING ORGANIZATION NAME AND ADDRESS Metallurgy Division National Bureau of Standards Gaithersburg, MD 20899		10. PROGRAM ELEMENT, PROJECT, TASK AREA & WORK UNIT NUMBERS 4D10 61101E
11. CONTROLLING OFFICE NAME AND ADDRESS Materials Science Division Defense Advanced Research Projects Agency 1400 Wilson Boulevard Arlington, VA 22209		12. REPORT DATE August 1984
11. CONTROLLING OFFICE NAME AND ADDRESS RING AGENCY NAME & ADDRESS (if different from Controlling Office)		13. NUMBER OF PAGES 70
		15. SECURITY CLASS. (of this report)
		15a. DECLASSIFICATION/DOWNGRADING SCHEDULE

ABSTRACT STATEMENT (of this Report)

Report is available for public release. Distribution unlimited.

ABSTRACT STATEMENT (of the abstract entered in Block 20, if different from Report)

DTIC
SELECTED
OCT 1 1984

15. SUPPLEMENTARY NOTES

19. KEY WORDS (Continue on reverse side if necessary and identify by block number)

Al-Mn alloys; Alloy microstructures; Non-planar interface morphology;
Precipitation; Rapid solidification; Solidification theory

20. ABSTRACT (Continue on reverse side if necessary and identify by block number)

Solidification theory can be used to predict and control processes occurring during rapid solidification. Two papers prepared for publication provide results showing such predictions. (1) Interface shapes and compositional fields produced during directional solidification, calculated as a function of solidification velocity, are reported. (2) Rapid solidification microstructures and precipitation produced upon annealing in rapidly solidified Al-Mn alloys having compositions in the extended solid solubility range are reported.

Application of Solidification Theory to
Rapid Solidification Processing

W. J. Boettinger, J. W. Cahn, S. R. Coriell,
J. R. Manning, and R. J. Schaefer
Metallurgy Division
Center for Materials Science
National Bureau of Standards
Gaithersburg, MD 20899

Semi-Annual Technical Report
Period Covered: October 1, 1983 to March 31, 1984

Report Issued: August 1984

Prepared for
Defense Advanced Research Projects Agency
Arlington, VA 22209

Program Code No: 4D10
Effective Date of Contract: April 1, 1979
Contract Expiration Date: September 30, 1986
Principal Investigator: J. R. Manning (301/921-3354)

"The views and conclusions contained in this document are those of the authors and should not be interpreted as representing the official policies, either expressed or implied, of the Defense Advanced Research Projects Agency or the U.S. Government."

Table of Contents

	Page
1. Task Objective	1
Technical Problem and General Methodology	1
Technical Results	2
2. Appendix - Papers Reporting Detailed Results	
Nonplanar Interface Morphologies during Unidirectional Solidification of a Binary Alloy	4
Rapid Solidification Microstructures and Precipitation in Al-Mn Alloys	30
Precipitation in Rapidly Solidified Al-Mn Alloys	35

Accession For	
NTIS GRA&I	<input checked="" type="checkbox"/>
DTIC TAB	<input type="checkbox"/>
Unannounced	<input type="checkbox"/>
Justification	
By	
Distribution/	
Availability Codes	
Dist	Avail and/or Special
A-1	



Application of Solidification Theory to

Rapid Solidification Processing

This semi-annual technical report for ARPA Order 3751 covers the period October 1, 1983 to March 31, 1984.

Task Objective

The objective of this work is to develop guidelines based on kinetic and thermodynamic solidification theory for prediction and control of rapid solidification processes. In particular, segregation effects and rules governing the formation of equilibrium and non-equilibrium phases, will be investigated. Areas where significant improvements in alloy properties can be produced by rapid solidification will be emphasized.

Technical Problem and General Methodology

Rapid solidification techniques make it possible to produce new types of materials having significantly better properties than conventionally processed materials. However, improved predictive techniques and control of rapid solidification processes are needed. The current studies are focussed on the science underlying areas where improved materials can be obtained in order to provide such prediction and control. This work is both theoretical and experimental.

Ways in which rapid solidification produces special properties in alloys include:

- A. Enhanced homogeneity, improved microstructures
 - creates more uniform alloys and allows formation of fine precipitates with resulting improvements in mechanical properties.

B. Extended solid solubility

- provides alloys with high solute content, not normally available to design engineers.

Significant accomplishments have been achieved during the course of this contract in each of these areas.

Technical Results

(1) Enhanced homogeneity, improved microstructures

The microstructures obtained by rapid solidification depend strongly on the solidification velocity. Thus, rapid solidification can provide unique properties to alloys even when dendritic solidification of equilibrium (stable) phases occurs. During any non-partitionless and non-planar solidification process, alloy segregation can be expected in the resulting solid. Resulting alloy properties depend on the type of segregation obtained. Key questions are, "What are the interface shape, temperature and compositional fields produced during rapid solidification, especially when there are non-equilibrium interface conditions?" and "How do these influence the interdendritic spacings and segregation effects that are obtained during rapid solidification?"

A paper resulting from the present work which reports some detailed calculations on this topic is:

- (A) Nonplanar Interface Morphologies during Unidirectional Solidification of a Binary Alloy, G. B. McFadden and S. R. Coriell, Physica (1984).

This paper is included in the appendix as part of this report.

(2) Extended solid solubility

At rapid solidification velocities, there often is not enough time during

the freezing process for the alloy species to separate into different phases. Thus, at alloy compositions where conventional solidification conditions produce two-phase alloys, rapid solidification processing may instead produce homogeneous alloys having solute contents much beyond the normal solubility limits. Key questions here are, "How rapid must the solidification rate be in order to produce solute trapping and partitionless solidification?" and "What subsequent microstructural changes and precipitation processes occur in these extended solid solubility alloys?"

Two papers resulting from the present work and reporting detailed studies on aluminum-manganese alloys are:

- (B) Rapid Solidification Microstructures and Precipitation in Al-Mn Alloys, R. J. Schaefer, D. Shechtman, and F. S. Biancaniello, (to be published in Proceedings of Materials Research Society Annual Meeting, held November 1983).
- (C) Precipitation in Rapidly Solidified Al-Mn Alloys, D. Shechtman, R. J. Schaefer, and F. S. Biancaniello (submitted to Metallurgical Transactions).

These papers are included in the appendix as part of this report. The work was done in collaboration with D. Shechtman, Johns Hopkins University, during time which he spent working at the National Bureau of Standards.

NONPLANAR INTERFACE MORPHOLOGIES DURING UNIDIRECTIONAL SOLIDIFICATION OF A BINARY ALLOY

G. B. McFadden and S. R. Coriell
National Bureau of Standards
Washington, DC 20234

ABSTRACT

During directional solidification of a binary alloy, a planar solid-liquid interface may become unstable and develop into a cellular non-planar interface, exhibiting periodic structure transverse to the growth direction. Steady state two-dimensional temperature, solute concentration, and interface shapes are calculated numerically and the solute inhomogeneity (microsegregation) in the solidified material obtained. Specific results are presented for an aluminum alloy containing silver for solidification velocities of 0.01 and 1.0 cm/s, which correspond to the constitutional supercooling and absolute stability regimes, respectively.

Introduction

Directional solidification is an established method for the production of alloys of technological importance [1-6]. In this process, there is uniform relative motion of the alloy sample and its thermal environment, so that at steady state the solid-liquid interface propagates at constant velocity. Growth velocities range from 10^{-4} to 1 cm/s with temperature gradients up to 500 K/cm. At equilibrium, the solute concentration in the liquid is different from the solute concentration in the solid. Thus, there is either rejection or preferential incorporation of solute by the solid at a moving solid-liquid interface; this leads to a concentration gradient in the liquid in the vicinity of the solid-liquid interface.

For a planar-crystal melt interface moving at constant velocity, there is a simple solution for which the temperature and concentration fields depend

only on the distance from the interface, and the resulting solid is of uniform composition. When the planar interface is unstable, the composition of the solid is non-uniform with spatial inhomogeneities of the order of $10\text{ }\mu\text{m}$ (microsegregation). In this paper, we investigate the nature of the planar to cellular transition and examine its dependence on parameters that can be controlled during solidification.

A treatment of the linear stability of a planar interface was given by Mullins and Sekerka in 1964 [7], see also [8], which extended the constitutional supercooling criterion originally given in [2]. A further analysis by Coriell et.al. includes the effects of convection in the liquid [9]. Nonlinear stability analyses have been performed for the two-dimensional case by Wollkind and Segel [10], and Dee and Mathur [11], and for the three-dimensional case by Sriranganathan et.al. [12]. Kerszberg [13] computes several terms in a modal expansion of the interface and considers the question of wavelength selection. Studies of the dependence of the concentration field on a given nonplanar interface shape have been performed by Carlson et.al. [14], Coriell and Sekerka [15], and Coriell et.al. [16]. A nonlinear free boundary problem in crystal growth has been studied using finite elements by Ettouney and Brown [17]. In that work the interface shape is determined by heat transfer effects, and the concentration field is computed once the interface location is known.

The method to be presented here is a finite difference formulation of the equations describing diffusion of solute in the liquid and diffusion of heat in the liquid and solid. A self-consistent interface location is computed by an iterative procedure that effectively introduces an artificial time de-

pendence in the problem. The procedure reproduces the correct linear instabilities for the planar interface, and computes nonplanar steady state solutions in the limit of large artificial time. The results described here correspond to the two-dimensional case, although the method is equally applicable to three dimensions. Finite element methods are being applied to this problem by Ungar and Brown [18].

Theory

We consider solidification at constant velocity V in the \bar{Z} direction, and choose a coordinate system (\bar{X}, \bar{Z}) moving with the interface. We assume the steady state interface shape can be expressed in the form $\bar{Z} = \bar{W}(\bar{X})$. The temperature and solute concentration in the liquid region $\bar{Z} > \bar{W}(\bar{X})$ are denoted by \bar{T} and \bar{C} , and the temperature in the solid region $\bar{Z} < \bar{W}(\bar{X})$ is denoted by \bar{T}_s . We assume that no diffusion of solute occurs in the solid, since typical values of the solute diffusion coefficient are generally orders of magnitude smaller in the solid than in the liquid. The concentration of solute in the solid is given by its values at the interface $\bar{Z} = \bar{W}(\bar{X})$. The equations governing conservation of solute and heat are then

$$(1) \quad -V\partial\bar{C}/\partial\bar{Z} = D \left((\partial^2\bar{C}/\partial\bar{X}^2) + (\partial^2\bar{C}/\partial\bar{Z}^2) \right), \quad \bar{Z} > \bar{W}(\bar{X})$$

$$(2) \quad -V\partial\bar{T}/\partial\bar{Z} = K \left((\partial^2\bar{T}/\partial\bar{X}^2) + (\partial^2\bar{T}/\partial\bar{Z}^2) \right), \quad \bar{Z} > \bar{W}(\bar{X})$$

$$(3) \quad -V\partial\bar{T}_s/\partial\bar{Z} = K_s \left((\partial^2\bar{T}_s/\partial\bar{X}^2) + (\partial^2\bar{T}_s/\partial\bar{Z}^2) \right), \quad \bar{Z} < \bar{W}(\bar{X})$$

The constants D , K , and K_s are solute diffusivity in the liquid and thermal diffusivity in the liquid and solid, respectively. We will assume that the thermal properties of the liquid and solid are the same, so that $K = K_s$.

We assume that during the phase change local equilibrium is maintained at the solid liquid interface. The Gibbs-Thomson equation,

$$(4) \quad \bar{T} = T_m + M\bar{c} - T_m r K \text{ at } \bar{Z} = \bar{W}(\bar{X})$$

then relates the temperature, concentration of solute in the liquid, and interface mean curvature K . Here T_m is the melting point of the pure material ($c = 0$), and r is a capillary length. M is the slope of the liquidus curve and gives the alteration of melting point due to the presence of solute. The temperature is continuous at the interface,

$$(5) \quad \bar{T} = \bar{T}_s \text{ at } \bar{Z} = \bar{W}(\bar{X}),$$

while there is a jump in concentration across the interface. The phase diagram implies the relation $\bar{c}_s = \tilde{k}\bar{c}$, where the distribution coefficient \tilde{k} is the ratio of solute concentration in the solid to that in the liquid. Conservation of energy is expressed by the condition

$$(6) \quad -LV_n = k((\partial\bar{T}/\partial\bar{v}) - (\partial\bar{T}_s/\partial\bar{v})), \text{ at } \bar{Z} = \bar{W}(\bar{X})$$

where L is the latent heat per unit volume released upon solidification, k is the thermal conductivity in the liquid and solid, and the normal component of the velocity $V_n = V_z$. The normal derivative $\partial/\partial\bar{v}$ is taken with $\bar{v} = (\bar{v}_x, \bar{v}_z)$ pointing into the liquid. Conservation of solute at the interface takes the form

$$(7) \quad D \partial\bar{c}/\partial\bar{v} = -V_n(1 - \tilde{k})\bar{c}, \text{ at } \bar{Z} = \bar{W}(\bar{X})$$

The solution to equations (1)-(7) corresponding to a planar interface $\bar{Z} = \bar{W}(\bar{X}) = 0$ are

$$(8) \quad \bar{c}(\bar{Z}) = c_\infty [1 + ((1 - \tilde{k})/\tilde{k}) \exp(-V\bar{Z}/D)]$$

$$(9) \quad T(Z) = T_m + M c_\infty / \tilde{k} + (KG_L/V) [1 - \exp(-VZ/K)]$$

$$(10) \quad \bar{T}_s(\bar{Z}) = T_m + Mc_\infty/\tilde{k} + (K/V)(G_L + LV/k) [1 - \exp(-V\bar{Z}/K)]$$

where c_∞ is the solute concentration far from the interface and G_L is the temperature gradient in the liquid at the interface. If the solution (8)-(10) is unstable, there may be additional solutions to the system (1)-(7) that satisfy the same far-field boundary conditions and are periodic in the \bar{X} -direction.

Numerical Method

Although the equations (1)-(3) are linear, the boundary conditions (4)-(7) are nonlinear in the concentration and temperature fields and the unknown interface location $\bar{Z} = \bar{W}(\bar{X})$. We employ an iterative approach that is similar to methods used in other free boundary problems [19-20]. The procedure is started with a guess for the interface location; for example, a slightly perturbed planar interface or the interface obtained in a previous calculation using different growth conditions. For this location of the interface, the solute and temperature fields are computed using equations (1)-(3) with boundary conditions (5)-(7) and appropriate far-field boundary conditions. For the assumed interface location, the Gibbs-Thomson equation (4) will generally not be satisfied. The Gibbs-Thomson equation is used to generate an improved estimate for the interface shape, and the procedure is then repeated until a given convergence criterion is met. The successive approximations generate a sequence of fields and interface shapes that can be viewed as an evolution in artificial time to a steady state that satisfies the equations (1)-(7).

For a given periodic interface shape $\bar{z} = \bar{w}(X)$ with fixed wavelength λ , the concentration field is computed as follows. If the length scale is non-dimensionalized by λ and the concentration field by c_∞ , the equations are

$$(11) \quad \beta \partial c / \partial z + \partial^2 c / \partial x^2 + \partial^2 c / \partial z^2 = 0 \quad , \quad H_c > z > w(x)$$

$$(12) \quad \partial c / \partial \eta + \frac{1}{z} \beta (1 - \tilde{k}) c = 0 \quad , \quad z = w(x)$$

$$(13) \quad \partial c / \partial z + \beta c = \beta \quad , \quad z = H_c$$

$$(14) \quad \partial c / \partial x = 0 \quad , \quad x = 0, 1/2.$$

Here the parameter $\beta = V\lambda/D$, and the height H_c is chosen large enough that the concentration is independent of H_c and is uniform in x near $z = H_c$. The boundary condition (13) gives the proper far field behavior seen in (8) and also insures overall conservation of solute [16]. For large β , a boundary layer of width $O(1/\beta)$ is formed near $z = w(x)$. The domain $w(x) < z < H_c$ is mapped to a rectangular computational domain by the sequence of transformations

$$(15) \quad \begin{aligned} \tilde{x} &= x \\ \tilde{z} &= H_c (z - w(x)) / (H_c - w(x)), \end{aligned}$$

$$(16) \quad \begin{aligned} \xi &= \tilde{x} \\ \eta &= 1 - \exp(-\beta \tilde{z}). \end{aligned}$$

The transformed equation (11) for $C(\xi, \eta)$ takes the form

$$(17) \quad (eC_\xi + fC_\eta)_\xi + (fC_\xi + gC_\eta + \beta C)_\eta = 0$$

where

$$e = (H_c - w(\xi)) / (\beta H_c (1 - n))$$

$$f = - (1 - (\tilde{z}/H_c)) w'(\xi)$$

$$g = \beta H_c (1 - n) (1 + (1 - (\tilde{z}/H_c)^2) w'(\xi)^2) / (H_c - w(\xi)).$$

Equation (17) is approximated by second-order accurate central differences for $C_{ij} = C(i\Delta\xi, j\Delta n)$, using discrete values $w_i = w(i\Delta\xi)$ in the coefficients e , f , and g . An approximate solution to the finite difference equations is obtained at each step of the overall iteration scheme by using 10-20 sweeps of an alternating-direction-implicit method [21]. The results were checked independently using the ELLPACK software system [22].

The temperature is made dimensionless by the factor λG_L . The dimensionless temperature equations are

$$(18) \quad \alpha \partial T / \partial z + \partial^2 T / \partial x^2 + \partial^2 T / \partial z^2 = 0, \quad H_T > z > w(x)$$

$$(19) \quad \alpha \partial T_s / \partial z + \partial^2 T_s / \partial x^2 + \partial^2 T_s / \partial z^2 = 0, \quad -H_T < z < w(x)$$

$$(20) \quad T = T_H, \quad z = H_T$$

$$(21) \quad T_s = T_c, \quad z = -H_T$$

$$(22) \quad \begin{cases} T - T_s = 0 \\ \partial T / \partial v - \partial T_s / \partial v = -LV_n / (kG_L) \end{cases}, \quad z = w(x)$$

$$(23) \quad \partial T / \partial x = \partial T_s / \partial x = 0, \quad x = 0, 1/2,$$

where $\alpha = V\lambda/K$, and the constants T_H and T_C correspond to the temperatures of the planar solution (9) and (10) far from the interface at $z = H_T$ and $z = -H_T$, respectively. We remove the discontinuous behavior of the temperature gradient at the interface by introducing the auxiliary temperature field

$$T_p(x, z) = \begin{cases} 0, & z > w(x) \\ (LV/(kG_L)) (z - w(x))/(1 + w'(x)^2) \\ + 1/2 A'(x) (z - w(x))^2, & z < w(x) \end{cases}$$

where $\Lambda(x) = - (LV/(kG_L)) [\alpha + w'(x)^2 (\alpha + 3w''(x)) - w''(x)] / (1 + w'(x)^2)^3$.

The function

$$\tilde{T}(x, z) = \begin{cases} T(\lambda, z) - T_p(x, z), & z > w(x) \\ T_s(x, z) - T_p(x, z), & z < w(x) \end{cases}$$

is then twice continuously differentiable for $-H_T < z < H_T$ and satisfies an equation

$$(24) \quad \alpha \partial \tilde{T} / \partial z + \partial^2 \tilde{T} / \partial x^2 + \partial^2 \tilde{T} / \partial z^2 = \tilde{F}(x, z), \quad -H_T < z < H_T.$$

where \tilde{F} is a continuous function of x and z which follows from the preceding definitions. We use the fast elliptic solver GENBUN from the FISHPACK library [23] to solve this separable equation. Values of \tilde{T} along the interface $z = w(x)$ are obtained by interpolation in z with cubic splines [24] along each vertical line $x = i\Delta x$.

Given approximations $w^{(n)}$, $C^{(n)}$, and $T^{(n)}$ to the solution, an $(n+1)$ st approximation $w^{(n+1)}$ is obtained from the Gibbs-Thomson equation

$$(25) \quad 0 = T_m / (\lambda G_L) + (Mc_\infty / (\lambda G_L)) C + (T_m \Gamma / (\lambda^2 G_L)) w''(x) (1 + w'(x)^2)^{-3/2} - T \\ = F[w, w', w''],$$

where the functional F depends both explicitly and implicitly on $w(x)$ through the fields C and T . The updated value is computed in the form

$$(26) \quad a w_{tt} + b w_t = F,$$

$$\text{where } w_{tt} = (w_i^{(n+1)} - 2w_i^{(n)} + w_i^{(n-1)})/\Delta t^2$$

$$w_t = (w_i^{(n+1)} - w_i^{(n)})/\Delta t, \text{ and } F = F_i^{(n)} \text{ is obtained from } C^{(n)}, T^{(n)}, \text{ and } w^{(n)}.$$

Second-order accurate central differences are used for w and w' in the curvature term. We take $\Delta t = \Delta x$, $a = T_m r/(\lambda^2 G_L)$, and choose b empirically so that the iterates converge rapidly [19] to a steady state corresponding to $w_t = w_{tt} = 0$ in (26).

A linear stability analysis of the planar solution (8)-(10) to the artificially time dependent system (11)-(14), (18)-(23), and (26) shows that the conditions for marginal stability are identical to those corresponding to the time dependence in the true physical problem [8]. A perturbation of the unstable planar solution can then lead to a computed nonplanar solution with finite amplitude distortions in the interface shape.

Most of the results shown here are obtained on a mesh of 32×32 points in each of the liquid and solid regions. The solution is computed over half a wavelength in the horizontal direction. Running time on the NBS Univac 1100/82 using single precision arithmetic is approximately thirty minutes for the full development of a nonplanar solution from an unstable planar interface. Convergence typically proceeds as shown in fig. 1, where the solid curve shows the logarithm of the maximum residual of the Gibbs-Thomson

equation as a function of iteration number, and the two dotted curves show the development of the first two Fourier components of the interface shape.

Numerical Results and Discussion

We consider an aluminum-silver system [25] with the thermal properties of the solid taken to be identical to those of the actual liquid, see Table 1. The temperature gradient in the liquid is fixed at 100 K/cm. Fig. 2 shows linear stability results for the planar interface in terms of the critical bulk concentration C_{∞}^* as a function of the solidification velocity V . The planar interface is stable for bulk concentrations below the curve, and unstable for values above the curve. The left side of the curve corresponds to the constitutional supercooling criterion, while the curve rises on the right side due to the stabilizing effects of surface tension at higher velocities (absolute stability [7]). We present calculations of cellular interfaces for $V = .01$ cm/s and $V = 1.0$ cm/s.

For a given solidification velocity and imposed temperature gradient, the critical bulk solute concentration at the onset of instability depends on the wavelength λ of the sinusoidal perturbation of the interface. We refer to this curve as $C_{\infty}(\lambda)$ and denote the minimum value $C_{\infty}(\lambda^*)$ as C_{∞}^* ; C_{∞}^* was shown in fig. 2 as a function of solidification velocity V . For $V = 0.01$ cm/s, $C_{\infty}^* = 0.2235$ wt. % and $\lambda^* = 7.54(10^{-3})$ cm. For bulk concentrations higher than C_{∞}^* there is a range of linearly unstable wavelengths that is roughly centered about the marginal value λ^* . In fig. 3 we show the steady state interface shape for $C_{\infty} = .235$ wt. % and $\lambda = 6.0(10^{-3})$ cm, which is slightly smaller than the wavelength of the most unstable linear mode ($\lambda = 6.6(10^{-3})$ cm) at this concentration. The solute accumulation along the interface is highest in the

grooves of the cell, and the interface shape is distinctly non-sinusoidal, as is indicated by the Fourier coefficients shown in fig. 4. If we fix the wavelength of the cell at $\lambda = 6.0(10^{-3})$ cm and increase the bulk concentration from the marginal value for this wavelength, $C_{\infty}(\lambda) = .2258$ wt. %, the cell depth and solute distribution in the solid change as shown in fig. 5. The three plots represent solutions computed for $c_{\infty} = 1.005 C_{\infty}(\lambda)$, $c_{\infty} = 1.04 C_{\infty}(\lambda)$, and $c_{\infty} = 1.13 C_{\infty}(\lambda)$, respectively. The cell groove deepens and the accompanying solute segregation increases rapidly as the bulk concentration is raised.

If the bulk concentration is fixed at $c_{\infty} = .235$ wt. % and the wavelength of the cell is changed, the results shown in fig. 6 are obtained. The vertical axis gives the amplitude of the interface deformation in terms of the depth $(\max \bar{W}(\bar{X}) - \min \bar{W}(\bar{X}))/\lambda^*$. The range of linearly unstable wavelengths is $4.65(10^{-3}) \text{ cm} < \lambda < 1.32(10^{-2}) \text{ cm}$. Nonplanar solutions exist at wavelengths shorter than those predicted by linear theory. At $\lambda = 4.25(10^{-3})$ cm, for example, an initial sinusoidal perturbation of sufficiently large amplitude will develop into a nonplanar steady state, while the planar solution is stable to small perturbations. The marginal amplitude is indicated with a "+" in fig. 6. Different nonplanar solutions are obtained for $\lambda = 4.0(10^{-3})$ cm and $\lambda = 8.0(10^{-3})$ cm, so that there may be more than one solution with a given periodicity. Note that the maximum cell depth occurs for wavelengths smaller than λ^* . The fastest growing linear mode also shows a shift to shorter wavelengths.

An initial disturbance of wavelength $9.0(10^{-3})$ cm initially grows in accord with linear theory, and the first harmonic with half this wavelength is also

excited. Eventually, however, the main harmonic stops growing and then decays to zero amplitude, while the first harmonic asymptotes at a finite amplitude, resulting in a periodic solution with wavelength $\lambda = 4.5(10^{-3})$ cm. This behavior is observed for all wavelengths in the range $9.0(10^{-3}) \text{ cm} < \lambda < 13.1(10^{-3}) \text{ cm}$. The triangular data points shown in fig. 6 correspond to solutions whose initial perturbation of wavelength λ give rise to steady solutions with wavelength $\lambda/2$. These solutions are computed using 64 mesh points in the x-direction so that the number of mesh points per wavelength ($\lambda/2$) remains the same.

Figure 7 shows results similar to fig. 6, but corresponding to a solidification velocity of 1.0 cm/s and bulk concentration $c_{\infty} = .110$ wt. %, where $c_{\infty}^* = .099$ wt. % and $\lambda^* = 6.15(10^{-4})$ cm. The range of linearly unstable wavelengths is $4.33(10^{-4}) \text{ cm} < \lambda < 8.67(10^{-4}) \text{ cm}$, and the numerical procedure reproduces this range to within 1.6%. In contrast to the lower velocity, we have not found solutions outside the wavelength range indicated by linear stability theory. This difference between the two velocities is not unexpected based on the non-linear stability analysis of Wollkind and Segel [10].

Figure 8 shows the concentration field, temperature field, and interface shape for a sample with $c_{\infty} = .115$ wt. % and $\lambda = 5.0(10^{-4})$ cm. The distortion of the isotherms near the interface is due to the heat released by the liquid upon solidification. The concentration contours emphasize the large buildup of solute in the interface depression. The vertical lines in the solid indicate the extent of solute segregation; each band contains the same amount of solute.

Figure 9 shows the interface solute distribution in more detail. Note that the minimum concentration does not occur at the maximum of the interface. Solute distributions with local maxima of concentration at positions corresponding

to the peak of the solid-liquid interface have been observed experimentally at high growth velocities, and this has been attributed to non-equilibrium conditions prevailing at the interface [26]. It is interesting that a similar feature can be obtained under the equilibrium conditions assumed here.

These results indicate the extreme non-linearity of the cellular solidification problem. For example, in fig. 9 there is more than a factor of two difference between the maximum and minimum solute concentration in the solidified material for a bulk concentration 16% above the critical concentration. Even with the assumption of local equilibrium at the interface and equal thermal properties for solid and liquid, cellular solidification depends on six dimensionless parameters. A relatively small range of parameters has been investigated so far. We believe the steady state solutions we compute would also be obtained by integrating the true time-dependent equations. The numerical method used by Ungar and Brown [18] allows the computation of both stable and unstable solutions, and provides information about their linear stability as well. The stability of cell shapes of a given wavelength to perturbations of longer wavelength has not been examined here but is an area of active research [13], [27]. Time-dependent and three-dimensional calculations and methods to treat even greater degrees of non-linearity are areas for further research.

Acknowledgements

It is a distinct pleasure to acknowledge numerous contributions of R. F. Sekerka and R. F. Boisvert to various aspects of this problem. The authors have also benefited from conversations with W. J. Boettinger, R. A. Brown, G. Dee, M. Kerszberg, J. S. Langer, R. G. Rehm, R. J. Schaefer, and D. J. Wollkind. This work was supported in part by the Defense Advanced Research Projects Agency.

References

- [1] M. C. Flemings, Solidification Processing, McGraw-Hill, New York, (1974).
- [2] W. A. Tiller, J. W. Rutter, K. A. Jackson, and B. Chalmers, *Acta Met.* 1, (1953), p. 428.
- [3] R. F. Sekerka, Crystal Growth: An Introduction, edited by P. Hartman, North Holland, Amsterdam, (1973), p. 403.
- [4] R. T. Delves, Crystal Growth, Vol. 1, edited by B. R. Pamplin, Pergamon, Oxford, (1974), p. 40.
- [5] D. J. Wollkind, Preparation and Properties of Solid State Materials, Vol. 4, edited by W. R. Wilcox, Marcel Dekker, New York, (1979), p. 111.
- [6] J. S. Langer, *Rev. Mod. Phys.* 52, (1980), p. 1.
- [7] W. W. Mullins and R. F. Sekerka, *J. Appl. Phys.* 35, (1964), p. 444.
- [8] R. F. Sekerka, Crystal Growth, edited by H. S. Peiser, Pergamon, Oxford, (1967), p. 691.
- [9] S. R. Coriell, M. R. Cordes, W. J. Boettinger, and R. F. Sekerka, *J. Crystal Growth* 49, (1980), p. 13.
- [10] D. J. Wollkind and L. A. Segel, *Phil. Trans. R. Soc.* 268, (1970), p. 351.
- [11] G. Dee and R. Mathur, "Pattern Selection in Directional Solidification," *Phys. Rev. B.*, to be published.
- [12] R. Sriranganathan, D. J. Wollkind, and D. B. Oulton, "A Theoretical Investigation of the Development of Interfacial Cells During the Solidification of a Dilute Binary Alloy: Comparison with the Experiments of Morris and Winegard," to be published.
- [13] M. Kerszberg, *Phys. Rev. B* 27, (1983) p. 3909.
- [14] F. M. Carlson, L-Y. Chin, A. L. Fripp, and R. K. Crouch, Materials Processing in the Reduced Gravity Environment of Space, edited by G. E. Rindone, Elsevier Science Publishing, Inc., (1982), p. 629.
- [15] S. R. Coriell and R. F. Sekerka, *J. Crystal Growth* 46, (1979), p. 479.
- [16] S. R. Coriell, R. F. Boisvert, R. G. Rehm, and R. F. Sekerka, *J. Crystal Growth* 54, (1981), p. 167.

- [17] H. M. Ettouney and R. A. Brown, J. Crystal Growth, 58, (1982), p. 313.
- [18] L. H. Ungar and R. A. Brown, "Cellular Interface Morphologies in Directional Solidification," to be published.
- [19] F. Bauer, O. Betancourt, and P. Garabedian, A Computational Method in Plasma Physics, Springer-Verlag, New York, (1978).
- [20] P. R. Garabedian and G. B. McFadden, AIAA Journal 20, (1982), p. 289.
- [21] E. Isaacson and H. B. Keller, Analysis of Numerical Methods, Wiley and Sons, Inc., New York, (1966).
- [22] J. R. Rice, Mathematical Software III, edited by J. R. Rice, Academic Press, New York, (1977), p. 319.
- [23] P. N. Swarztrauber, SIAM J. Numer. Anal. 11, (1974), p. 1136.
- [24] C. de Boor, A Practical Guide to Splines, Springer-Verlag, New York, (1978).
- [25] R. J. Schaefer, W. J. Boettinger, F. S. Biancaniello, and S. R. Coriell, Lasers in Metallurgy, edited by K. Mukherjee and J. Mazumder, Metallurgical Society of AIME, (1981), p. 43.
- [26] T. Z. Kattamis, Z. Metallkde 61, (1970), p. 856.
- [27] G. Dee and J. S. Langer, Phys. Rev. Lett. 50, (1983), p. 383.

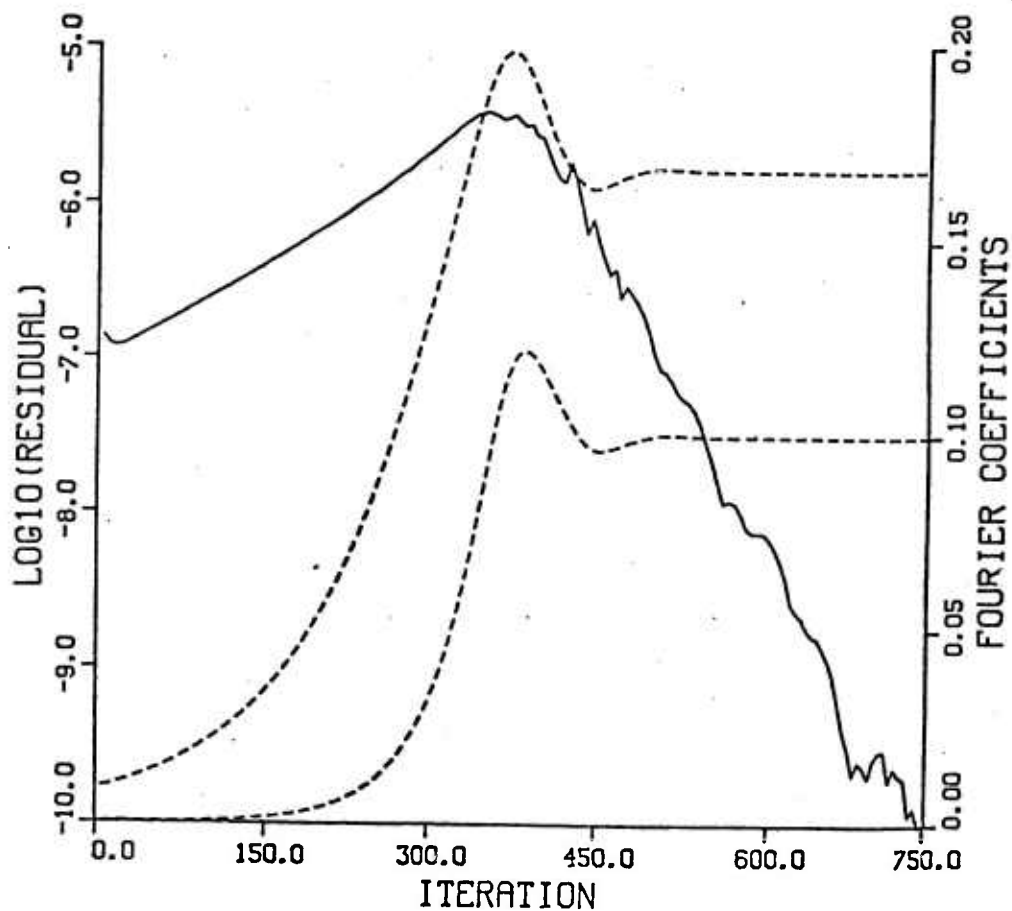
TABLE 1
Aluminum-Silver Properties
Used in Calculations

<u>Property</u>	<u>Symbol</u>	<u>Value</u>
Solute diffusion coefficient	D	$4.5(10^{-5}) \text{ cm}^2/\text{s}$
Distribution coefficient	\tilde{k}	0.4
Liquidus slope	M	-1.7 K/wt. %
Surface energy parameter	$\frac{T \Gamma}{m}$	$1.0(10^{-5}) \text{ cm} \cdot \text{K}$
Latent heat of fusion	L	$1.08(10^3) \text{ J/cm}^3$
Thermal conductivity of liquid	k	$9.04(10^{-1}) \text{ J}/(\text{s} \cdot \text{cm} \cdot \text{K})$
Thermal diffusivity of liquid	K	$3.52(10^{-1}) \text{ cm}^2/\text{s}$

Captions

- Figure 1 - Iterative convergence of the interface shape for $c_{\infty} = .235$ wt. %, $V = .01$ cm/s, and $\lambda = .005$ cm. The solid curve represents the base 10 logarithm of the maximum residual in the Gibbs-Thomson equation. The two-dotted curves show the amplitude of the main and first harmonic Fourier components of the interface shape.
- Figure 2 - The bulk silver concentration as a function of the interface velocity at the onset of linear instability for a planar interface in an aluminum-silver alloy. The planar interface is stable below the curve, unstable above it.
- Figure 3 - The interface shape and distribution of solute in the solid. The liquid is above and the solid is below the indicated interface. Two wavelengths are shown.
- Figure 4 - Fourier coefficients of the interface shape shown in fig. 3.
- Figure 5 - Plots of interface shape and distribution of solute in the solid for a given wavelength as the bulk concentration is increased. The top curve in each plot is the interface shape, the bottom curve is the concentration of solute. Two wavelengths are shown.
- Figure 6 - Maximum depth of the interface as a function of wavelength for $V = .01$ cm/s and $c_{\infty} = 1.05 C_{\infty}^*$. The range of linearly unstable wavelengths is indicated by crosses on the x-axis.
- Figure 7 - Maximum depth of the interface as a function of wavelength for $V = 1.0$ cm/s and $c_{\infty} = 1.11 C_{\infty}^*$.
- Figure 8 - Concentration and temperature contours in the liquid and solid for $V = 1.0$ cm/s and $c_{\infty} = 1.16 C_{\infty}^* = .115$ wt. %. The solid-liquid interface is shown also.
- Figure 9 - The interface shape and distribution of solute in the solid for the case shown in fig. 8. Two wavelengths are shown.

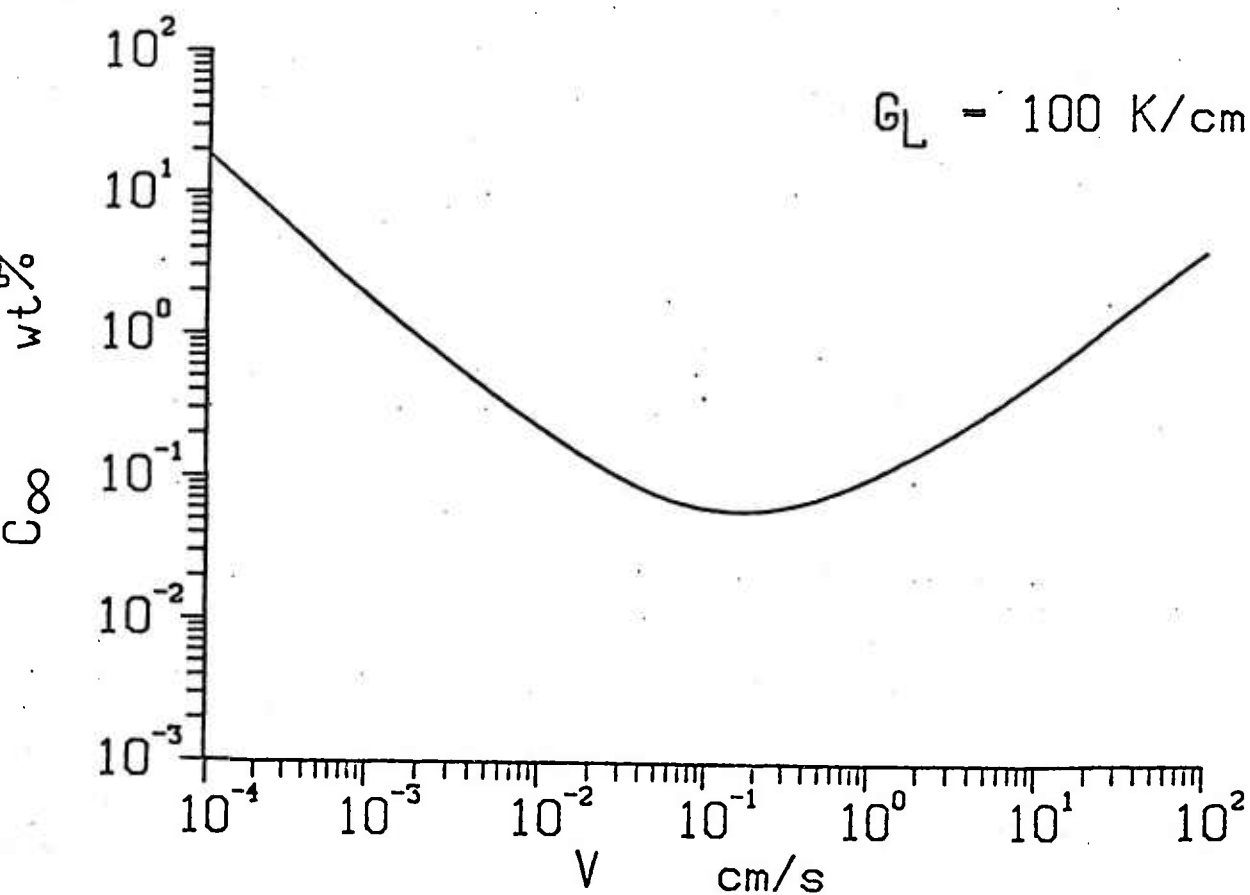
CONVERGENCE OF INTERFACE



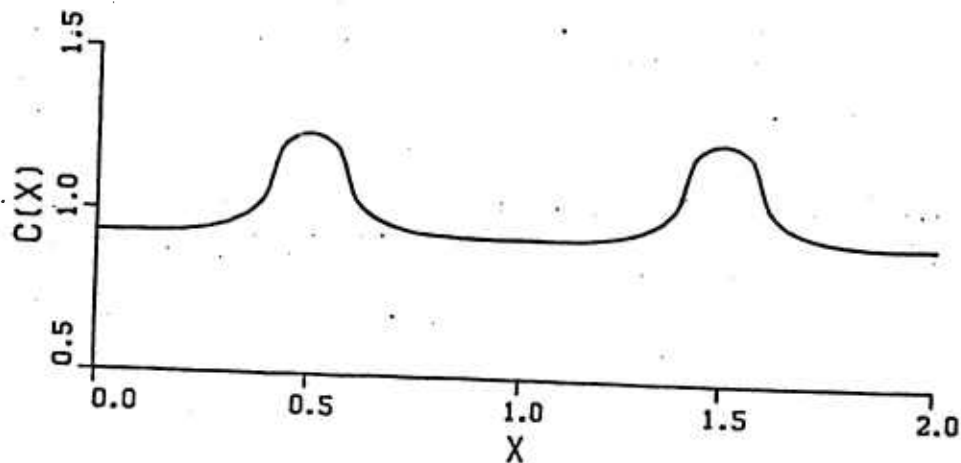
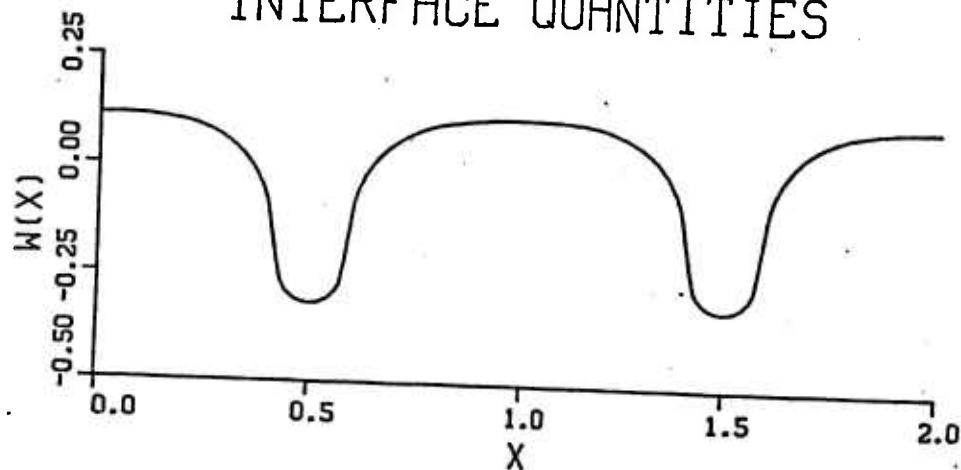
C -.235, V -.01 CM/S, L -.006 CM

FIGURE 1

LINEAR STABILITY FOR Al-Ag

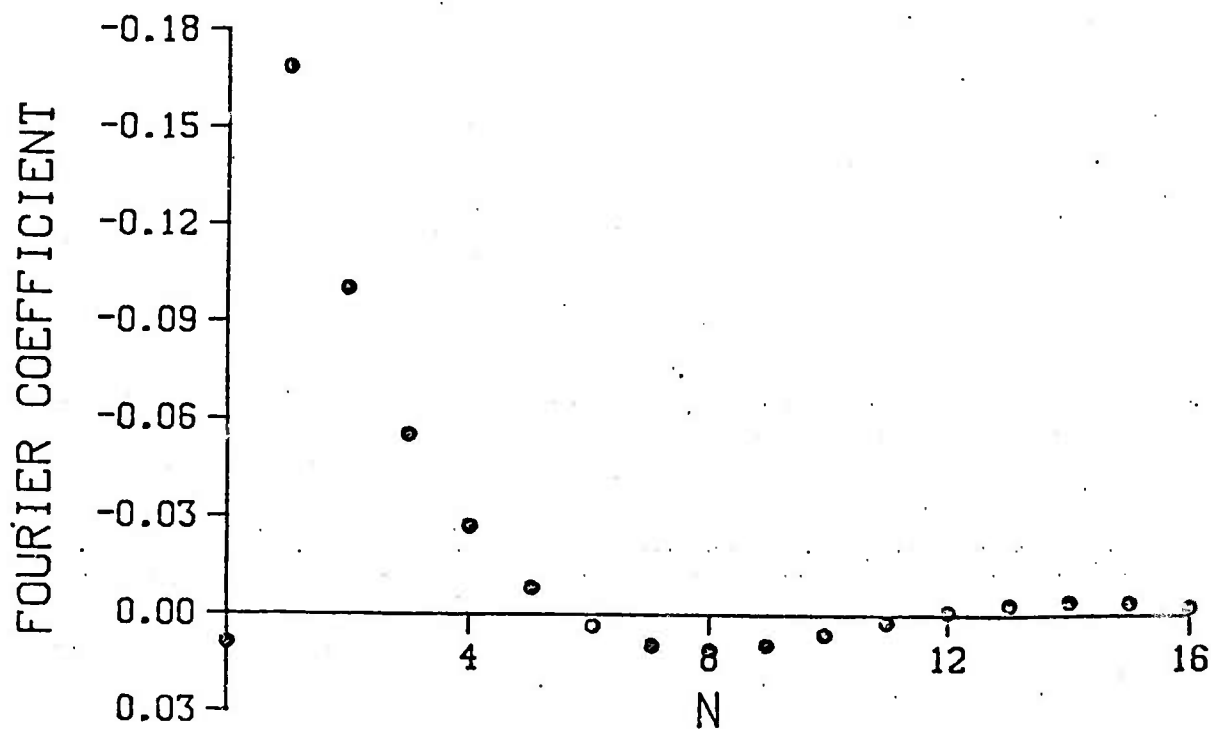


INTERFACE QUANTITIES



$C_{\infty} = .235$, $V = .01$ CM/S, $\lambda = .006$ CM

INTERFACE SHAPE FOURIER COEFFICIENTS



$$C_{\infty} = .235, \quad V = .01 \text{ CM/S}, \quad \lambda = .006 \text{ CM}$$

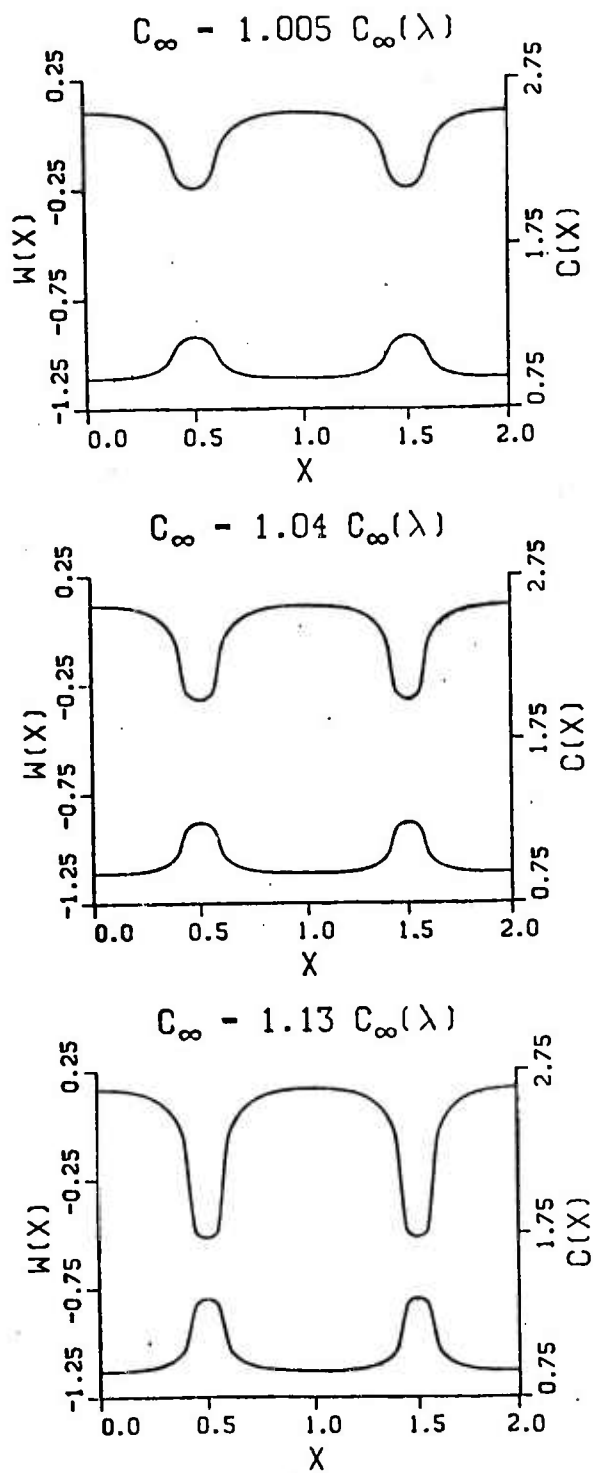


FIGURE 5

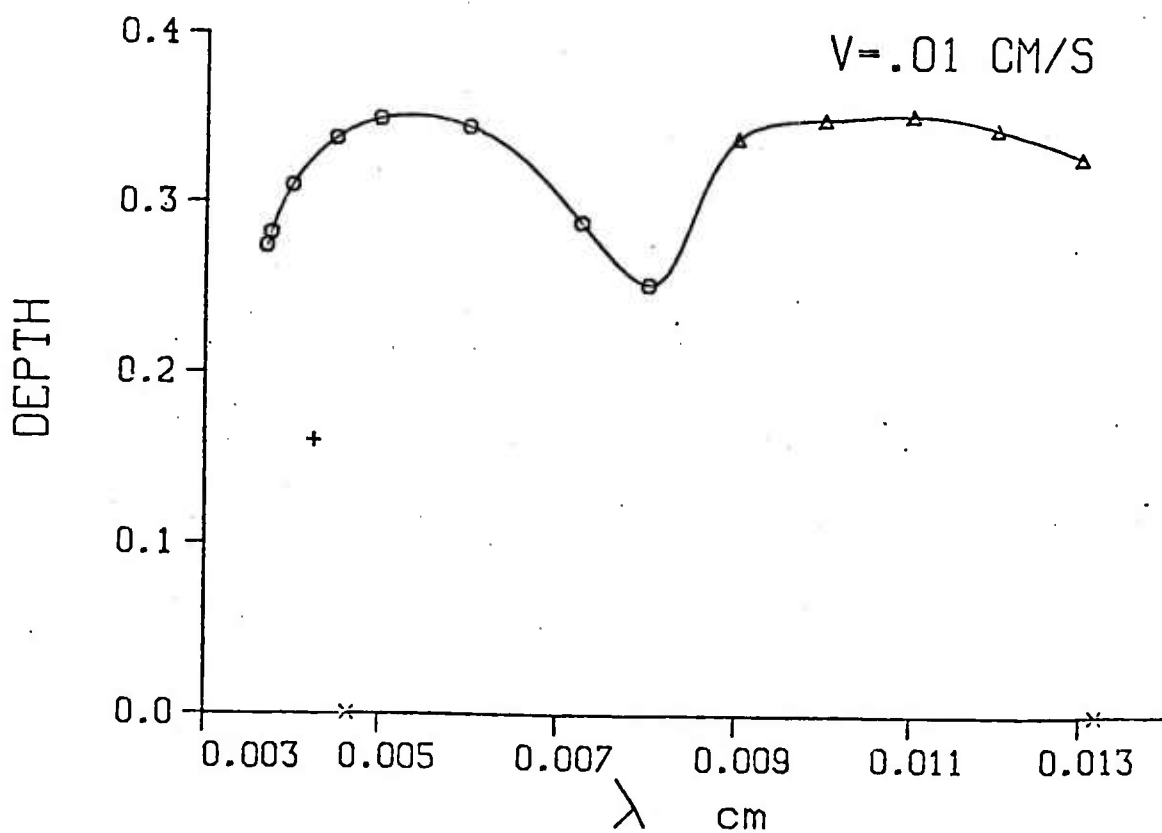


FIGURE 6

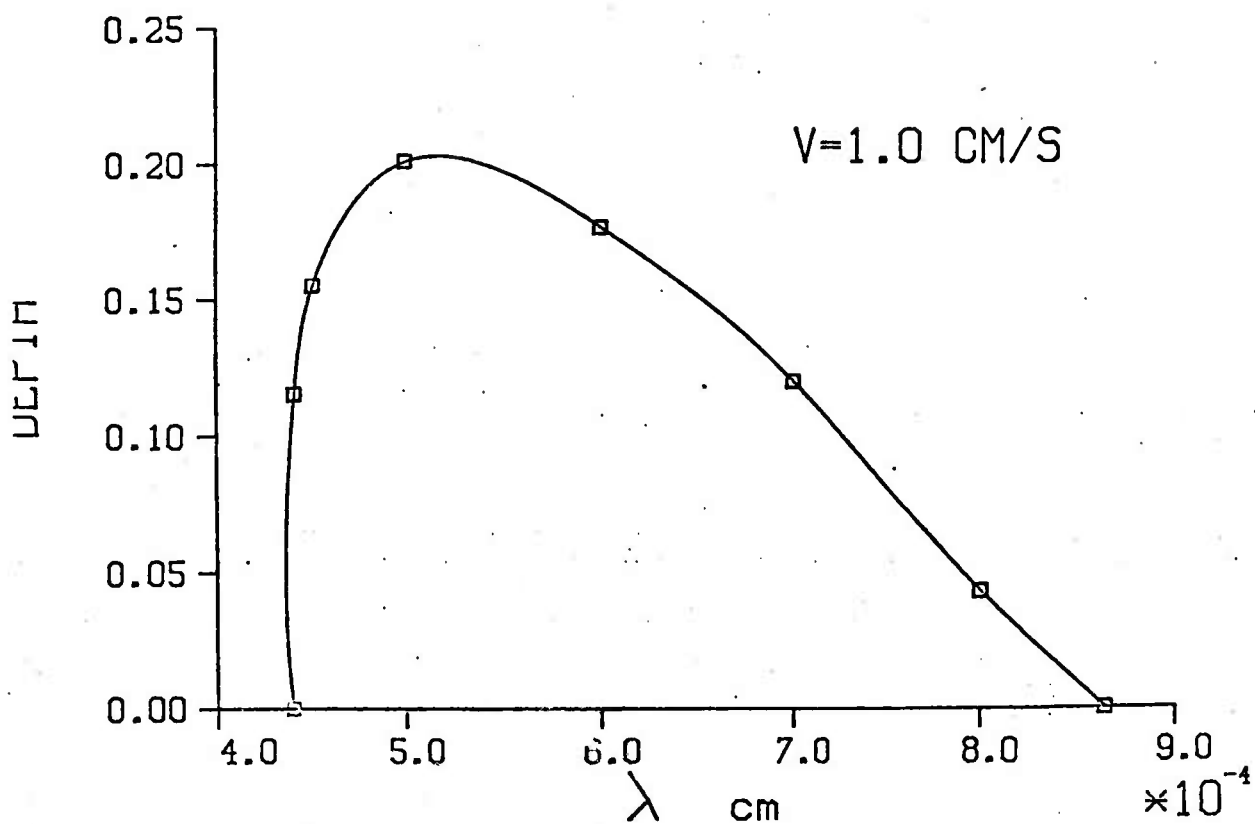
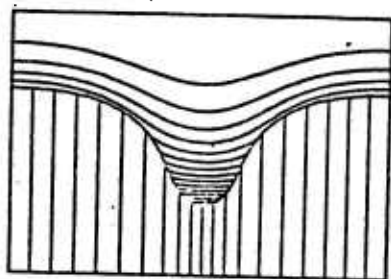
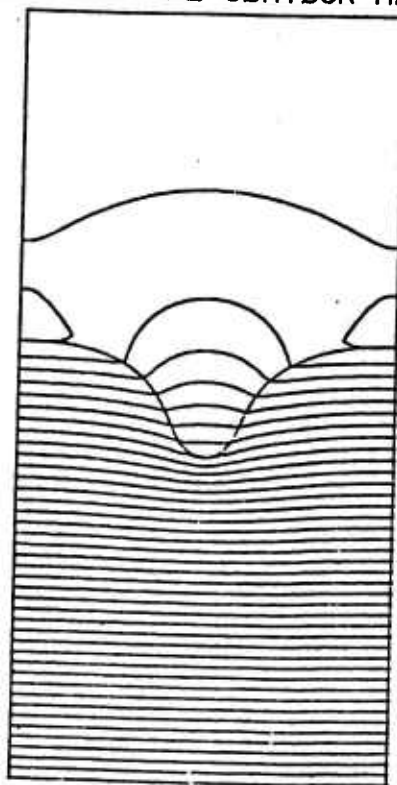


FIGURE 7

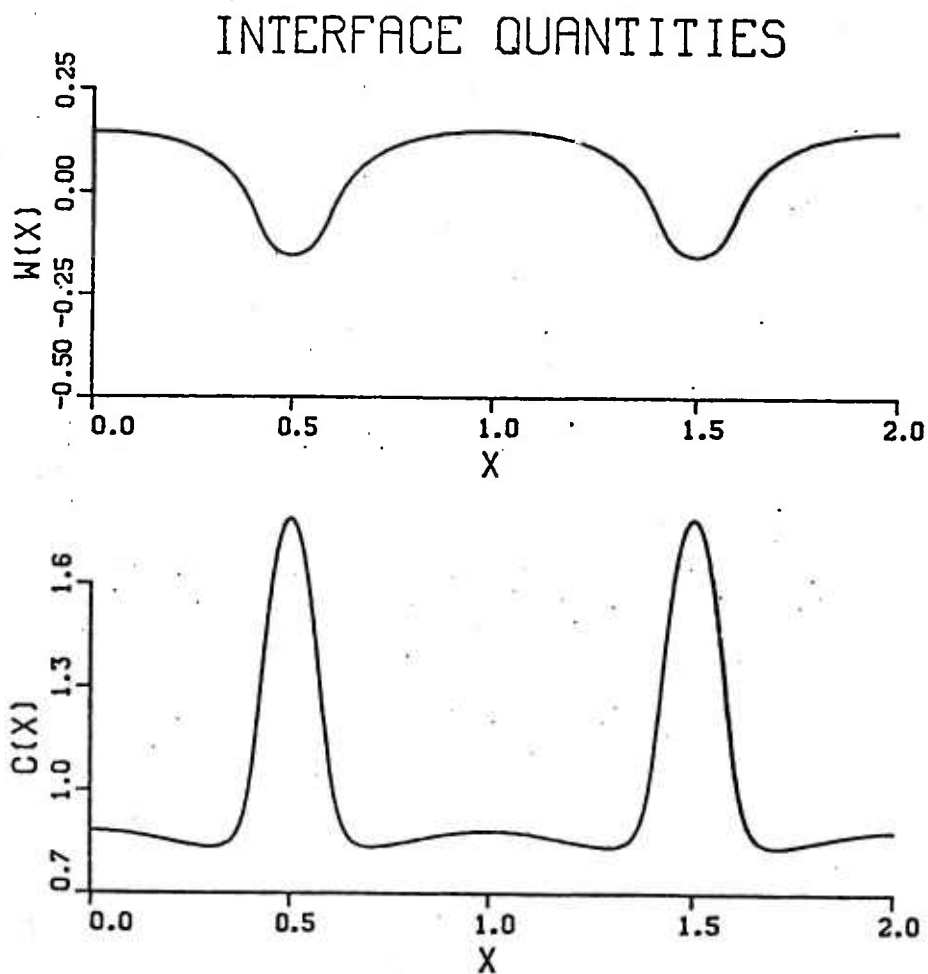
CONCENTRATION CØNTØUR MAP



TEMPERATURE CØNTØUR MAP



$$C = .1150, V = 1.000 \text{ CM/S}, L = .0005 \text{ CM}$$



$C_{\infty} = .115$, $V = 1.0$ CM/S, $\lambda = .0005$ CM

FIGURE 9

R. J. SCHAEFER*, D. SHECHTMAN**, AND F. S. BIANCANIELLO*
*National Bureau of Standards, Washington, D.C. 20234
**Technion, Haifa, Israel

ABSTRACT

Rapidly solidified Al containing up to 15 wt.% Mn was prepared by melt spinning. The alloys were examined by TEM and X-ray diffraction in the as-spun condition and after annealing at 450°C. Four precipitate phases were detected, and their growth kinetics were correlated to subgrain structures in the Al matrix.

INTRODUCTION

It has long been known that solid solutions containing far more than the limiting equilibrium concentration (1.4 wt.%) of Mn in Al can be obtained by rapid solidification [1]. Such solubility extensions in Al have been observed for almost every solute which has been investigated [2].

On the basis of interface equilibrium, the theory of morphological stability predicts an absolute stability regime in which plane-front microsegregation-free solidification of an alloy is stabilized by surface energy effects at sufficiently high solidification velocities. In the aluminum-manganese system the velocity required to produce this effect is predicted to be relatively low (a few centimeters per second) because of the high value of the solute partition coefficient [3]. In contrast, solutes with low distribution coefficients (Fe, Ni, Co, etc.) are predicted to be destabilizing at concentrations $\ll 1$ wt.% at comparable solidification velocities. Quantitative verification of the absolute stability effect has been observed in Ag-Cu alloys [4] but has not been reported for Al-based alloys. At solidification velocities approaching 1 m/s or greater, it is expected that interface equilibrium is no longer maintained, and microsegregation-free solidification can be attained even in systems having very low equilibrium partition coefficients [5].

When plane-front solidification is not stable, a cellular or dendritic interface develops and the solid which is generated contains a pattern of microsegregation. A network of crystal sub-boundaries can develop coincident with the microsegregation pattern, because of crystallographic mismatch between adjacent cells or dendrites.

During the annealing of supersaturated Al-Mn alloys the G phase, with composition corresponding to Al_{12}Mn and usually considered to be metastable, appears and at temperatures below about 500°C can persist for long times in samples which also contain the Al_6Mn phase [6]. In addition, Nes et al. [7] have reported two other metastable phases in Al-1.8 wt.% Mn annealed at 460°C. One phase, designated G', had a simple cubic structure, and the other phase, designated G'', had a hexagonal lattice with $c/a = 1.04$.

Unfortunately, none of the previous studies of precipitation in this system has covered the wide range of solid solution compositions which is attainable by rapid solidification. In this paper we report a study of precipitation at 450°C in melt-spun ribbons of Al-Mn containing up to 15 wt.% Mn.

EXPERIMENT

Melt-spun ribbons, typically 2 mm wide and 40-50 μm thick, were prepared from 99.999% Al and 99.95% Mn. Samples were annealed at 450° C for periods ranging from 5 minutes to 92 hours. Details of preparation are reported elsewhere [8]. Lattice parameters and the relative abundance of precipitate phases were determined from X-ray diffractometer measurements. Microstructural studies were performed in a 120 kv scanning transmission electron microscope.

RESULTS

Crystal Phases

In addition to the Al matrix, four phases have been identified by TEM in the as-spun or the annealed ribbons. The Al_6Mn phase is seen as generally globular particles with no preference in growth direction within the aluminum matrix. This phase occurs either on subgrain boundaries or within the subgrains depending upon composition and heat treatment. The G phase is semicoherent with the aluminum matrix and therefore is surrounded by misfit dislocations. The hexagonal G'' phase is faulted parallel to the basal plane, and the plate normal of the particles is parallel to the c direction. The T phase, which does not correspond to any previously reported phase, has the shape of an elongated plate and contains a complex faulted structure on planes perpendicular to its length. The G' phase of Nes et al. [7], which was believed to be associated with impurities, was not detected in our samples.

The X-ray diffraction charts show only peaks corresponding to reflections reported in the literature for Al_6Mn [9] and the G phase [6, 10, 11, 12], as well as Al.

As-spun Ribbons

At low Mn concentrations, the ribbons consist of cell-free grains containing a high dislocation density but no evidence of microsegregation. In the higher composition alloys, a cellular microstructure is present, with unidentified fine precipitates at the cell boundaries and a contrast difference between the cells indicating that the cell boundary is also a subgrain boundary. The transition from cell-free to cellular structures occurs at about 5 wt.% Mn. At this composition, two different ribbons were produced by varying the parameters of the melt spinning process. A thinner ribbon (35 μm maximum thickness) was free of cells while a thicker (55 μm) ribbon, which may have solidified more slowly, contained a cellular substructure.

The measured lattice parameters (Fig. 1) of the as-spun ribbons decrease with increasing Mn concentration as reported in several previous studies [1,13, 14,15], but in the cellular samples the decrease is not as large as would be expected if all of the Mn were in solid solution. In the 15 wt.% Mn ribbon diffraction peaks corresponding to two different concentrations of Mn in solution in Al are seen. These concentrations, approximately 14 and 3 wt.% Mn, correspond to a supersaturated cellular region and a two-phase solidification region respectively.

Annealed Ribbons

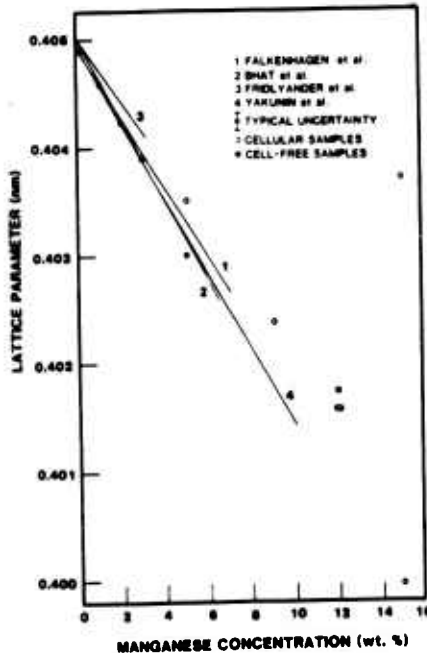


FIG. 1. Lattice parameters of as-spun Al-Mn ribbons compared to results of Falkenhagen et al.[1], Bhat, et al.[15], Fridlyander et al.[13], and Yakunin et al.[14].

At 450° C, the supersaturation of the alloys containing 5 wt.% Mn or more disappears rapidly. In contrast, the supersaturation of the alloys with 3 wt.% Mn or less diminishes over a period of many hours (Fig. 2). X-ray diffraction peaks from Al_6Mn are seen within one hour but the G phase peaks appear only after several hours. The G phase peaks increase in intensity with annealing time, while the Al_6Mn peaks diminish with time for anneals longer than 16 hours. On this basis, it appears that G is slightly more stable than Al_6Mn at 450° C. This is not inconsistent with the observations of other workers [6,16] who have investigated precipitation at this temperature in the Al-Mn system and have concluded that Al_6Mn is stable at high temperatures while the G phase persists for long times [6] or becomes stable [16] as the temperature decreases.

By TEM it is found that the location and growth kinetics of the different precipitating phases which form when the ribbons are annealed at 450° C are strongly correlated to the networks of subgrain boundaries which are present in the ribbons. These subgrain boundaries are already seen in the as-spun ribbons

at higher concentrations and are considered to be the result of the cellular solidification process. In the less concentrated alloys, where no cellular solidification structure is present, subgrain boundaries may be generated by polygonization.

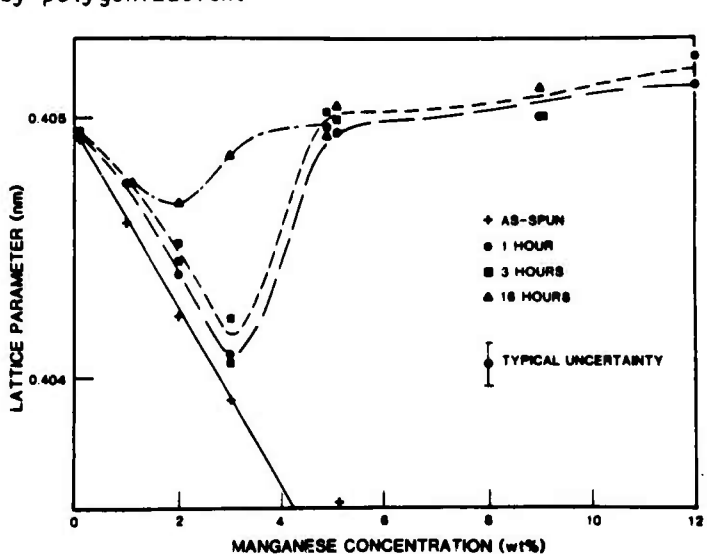


FIG. 2. Lattice parameter of Al-Mn ribbons at different annealing times.

In the 3 wt.% Mn alloy elongated particles of Al_6Mn are seen along subgrain boundaries after 1 hour at 450° C. The subgrains contain a high density of dislocations but only widely scattered precipitates. After 92 hours at 450° C, three precipitate phases are seen. All of them, including Al_6Mn , are now seen within the subgrains, possibly as a result of boundary migration. G phase particles, globular in shape, are surrounded by misfit dislocations indicating a high degree of coherence with the Al matrix. The G" Phase was in the form of elongated particles up to 2 μm in length.

The 5 wt.% Mn ribbons also showed Al_6Mn particles along the subgrain boundaries after being annealed for 1 hour. In addition, the interior of the subgrains showed a diffused population of T phase platelets except in a depleted zone adjacent to the subgrain boundaries (Fig. 3). In the thick ribbon, the Al_6Mn particles were more globular and the zone depleted of T particles was wider than in the thin ribbon. At longer annealing times considerable coarsening of the precipitate particles is seen.



FIG. 3. Al-5 wt.% Mn alloy following 1 hour anneal at 450°C.

The 9 wt.% Mn ribbon was examined after a 5 minute anneal and it was found that a globular phase was present along the subgrain boundaries and a needle-like phase was present within the subgrains. These phases could not be identified. The needle-like phase diminished in abundance as the annealing time increased, and after 16 hours it was found that Al_6Mn particles about 0.5 μm long were dispersed within the subgrains while large G phase particles outlined many of the subgrain boundaries.

At 12 wt.% Mn, a 1 hour anneal resulted in the formation of globular Al_6Mn particles within the Al matrix. After 22 hours at 450° C the microstructure consisted of an aluminum phase containing Al_6Mn particles and a G phase containing a low density of aluminum inclusions.

DISCUSSION

The microsegregation-free ribbons produced at compositions up to 5 wt.% Mn can be taken as evidence for a plane-front solidification process which is predicted by the theory of morphological stability to be stabilized at high solidification velocities. No quantitative correlation is possible because the actual velocities of solidification are not known. The onset of a cellular solidification process with increasing Mn content does not

preclude further increases in the supersaturation of the Al phase, but it does result in a microstructure containing a cellular array of subgrain boundaries which play an important role in subsequent precipitation processes.

Upon annealing at 450° C, precipitates lying along subgrain boundaries grow most rapidly. In the alloys containing 5 wt.% Mn or more, a high density of precipitates is seen within the subgrains but a denuded zone is present near the subgrain boundaries. These observations suggest that the subgrain boundaries serve as paths of rapid diffusion during the precipitation process.

In alloys containing 3 wt.% Mn or less, very few precipitates are formed within the grain and the supersaturation can thus persist for long times.

The G" phase and the T phase apparently occur only with a limited range of composition, and do not attain a sufficiently high volume fraction to be observed by X-ray diffraction. The G phase appears to be more stable than Al₆Mn at 450°C.

ACKNOWLEDGEMENT

This work was supported by DARPA.

REFERENCES

1. G. Falkenhagen and W. Hofman, *Z. Metal.* 43, 69 (1952).
2. H. Jones, *Aluminium* 54, 274 (1978).
3. R.J. Schaefer, S.R. Coriell, R. Mehrabian, C. Fenimore and F.S. Biancaniello, in *Rapidly Solidified Amorphous and Crystalline Alloys*, B.H. Lear, B.C. Giessen, and M. Cohen, eds., North Holland, New York, p. 79, 1982.
4. W.J. Boettinger, D. Shechtman, R.J. Schaefer, and F.S. Biancaniello, *Met. Trans* (in press).
5. J. Narayan, *J. Appl. Phys.* 52, 1289 (1981).
6. K. Little, G.V. Raynor, and W. Hume-Rothery, *J. Inst. Met.* 73, 83 (1946).
7. E. Nes, S.E. Naess, and R. Hoier, *Z. Metal.* 63, 248 (1972).
8. D. Shechtman, R.J. Schaefer, and F.S. Biancaniello, to be published.
9. A.D.I. Nicol, *Acta Cryst.* 6, 285 (1953).
10. K. Little and W. Hume-Rothery, *J. Inst. Met.* 74, 521 (1948).
11. G. Marchand, *J. Inst. Met.* 73, 747 (1947).
12. J. Adam and J.B. Rich, *Acta Cryst.* 7, 813 (1954).
13. I.N. Fridlyander, V.A. Konstantinov, and N.I. Zaitseva, *Zhurnal Fizicheskoi Khimii*, 30 (7), 1623 (1956).
14. A.A. Yakunin, I.I. Ostrov, V.I. Tkach, and A.S. Lysenko, *Fiz. Metal. Metalloved* 43, 140 (1977).
15. S.P. Bhat, T.R. Ramachandran, and A.K. Jena, *J. Mat. Sci.* 9, 1759 (1974).
16. K. Kusumoto and M. Ohta, *Journ. Inst. Polytechn. Osaka Univ.* 5 (6), 57 (1954); *Nippon Kinzoku Gakki-Si* 18 (8), 466 (1954).

PRECIPITATION IN RAPIDLY SOLIDIFIED Al-Mn ALLOYS

D. Shechtman⁺, R. J. Schaefer^{*}, and F. S. Biancaniello^{*}

⁺Dept. of Materials Engineering
Techion, Haifa, Israel
Currently on leave at the
Center for Materials Research
The Johns Hopkins University
Baltimore, MD 21218

^{*}National Bureau of Standards
Washington, DC 20234

ABSTRACT

Precipitation at 450°C was studied in melt-spun ribbons containing up to 15 wt.% Mn in solid solution in Al. The as-spun ribbons were microsegregation-free at compositions up to 5 wt.% Mn, but in more concentrated alloys a cellular microstructure was present. Upon annealing, four precipitate phases are observed, some of them being found preferentially on cell boundaries and others being found within the cells. Al₆Mn, G and the G" phase can coexist for long times at 450°C, but the G phase appears to be slightly more stable. A less stable I phase was detected in Al-5 wt.% Mn foils following short annealing periods. The supersaturation of the Al matrix can persist for many hours in alloys containing up to 3 wt.% Mn, but is essentially gone after 1 hour in alloys with 5 wt.% Mn or more.

I. INTRODUCTION

It has been known for many years that solid solutions containing far more than the limiting equilibrium concentration of manganese in aluminum can be obtained by rapid solidification [1]. A phase designated G, usually considered to be metastable and with composition corresponding to Al_{12}Mn , appears during the annealing of these supersaturated solutions, and at temperatures below about 500°C the G phase can persist for long times in samples which also contain the Al_6Mn phase [2]. Nes, et al., [3] have found two other metastable phases in Al-1.8 wt.% Mn annealed at 460°C . One phase was designated G'' and it has an hexagonal lattice with $c/a = 1.04$, and the other phase G' has a simple cubic structure. The Al-Mn system is of special interest because of the possibility that even concentrated alloys can freeze without microsegregation, as predicted by the theory of morphological stability [4], and because of the very slow rate at which phase equilibrium is established. Unfortunately, none of the previous studies of precipitation in this system has covered the wide range of solid solution compositions which is attainable by rapid solidification.

Extensive reviews [5,6,7] covering many aspects of the study of rapidly solidified aluminum alloys point out that a solid solubility extension has been observed in almost every system which has been investigated. For alloying elements such as Fe or Ni, which have extremely low maximum equilibrium solid solubilities in Al, the observed solubilities after rapid solidification lie far beyond any reasonable metastable extension of the solidus and thus indicate a non-equilibrium reaction at the solid-liquid interface. In contrast, manganese has a relatively high solubility in aluminum and if the formation of competing phases can be avoided, large extensions of the solubility limit would be expected even without any departure from equilibrium at the solid-liquid interface.

When an alloy solidifies by extraction of heat through the solid, as is normally the case in melt spinning, a microsegregation-free solid can be produced if the solid-liquid interface remains planar. If the planar interface is morphologically unstable, however, a cellular (or dendritic) microsegregation pattern can develop.

On the basis of interface equilibrium, the theory of morphological stability predicts an absolute stability regime in which plane-front microsegregation-free solidification of an alloy is stabilized by surface energy effects at sufficiently high solidification velocities. Such microsegregation-free solidification in the absolute stability regime has recently been demonstrated in Ag-Cu alloys [8]. In the aluminum-manganese system the velocity required to produce this effect is predicted to be relatively low because of the high value of the solute partition coefficient [9]. By this mechanism, rapid solidification processing could produce rather concentrated Al-Mn alloys without microsegregation. For example, a planar solid/liquid interface is predicted to be stable in an alloy containing 10 wt.% Mn when the solidification velocity is 6×10^{-2} m/s or greater, provided that at least a moderate positive temperature gradient is present in the liquid. At comparable solidification velocities, elements having low distribution coefficients (such as Fe) are predicted to be destabilizing even at concentrations $\ll 1$ wt.%. At solidification velocities in the range of 1 m/s or more, it is expected that the interface equilibrium is no longer maintained, and microsegregation-free solidification can be obtained even in systems having very low equilibrium partition coefficients [10].

The solidification microstructure plays an important role in the precipitation process in Al-Mn alloys because it influences the distribution of the various

precipitating phases. Because of the slow rate at which these phases displace one another, the solidification microstructure thus determines which of these phases dominates at various stages of annealing. We report here a study of the relationships between the microstructures formed in rapidly solidified Al-Mn alloys and the precipitation processes in these alloys.

II. EXPERIMENTAL

A. Sample Preparation

Alloy buttons with Mn concentrations of 0.1, 1, 2, 3, 5, 9, 12, and 15 wt.% Mn were prepared by arc melting, using 99.999% Al and 99.9% Mn. For melt spinning, small pieces cut from these buttons were induction heated in zirconia-coated quartz tubes. Immediately upon melting, the metal was spurted onto a copper melt-spinning wheel, 10 cm in diameter, which rotated at 100 rpm. The process was carried out under helium at atmospheric pressure. The ribbons were typically 2 mm wide and 40-50 μ m thick. For annealing at 450°C, the ribbons were sealed in borosilicate glass ampoules with 1/2 atmosphere of helium.

B. X-Ray Studies

Lattice parameters were determined by measurements on an x-ray diffractometer, using filtered $\text{CuK}\alpha$ radiation. A Nelson-Reiley procedure was used to obtain the lattice parameter from the measurements of the diffraction peaks. Simultaneous measurement of diffraction peaks from powdered high purity silicon were used as a normalization standard. The relative abundance of precipitate phases was evaluated semi-quantitatively by measuring the intensity of the strongest peaks.

C. Electron Microscopy

Microstructural studies were performed in a 120 kv scanning transmission electron microscope. The ribbons were thinned by jet electropolishing in a standard solution of 1.5% HNO_3 and 5% HClO_4 in methanol at -30 °C.

III. RESULTS

A. Phase Identification

Four phases have been identified by TEM in the as-spun and in the heat treated ribbons, in addition to the aluminum matrix. The crystallography of these phases will be shown now while their morphology and occurrence will be discussed later in this paper.

Al₆Mn - This phase is shown in Fig. 1. The particles are generally globular, and do not show any preference in growth direction within the aluminum matrix. They can be found either on subgrain boundaries or within the subgrains depending upon composition and heat treatment. The electron diffraction patterns obtained from this phase agree with its established crystallography [11] except for the (001) reflection which is forbidden by the symmetry of the crystal but clearly observed on the diffraction patterns. This may indicate a metastable structure of this equilibrium phase.

G Phase - This phase is semicoherent with the aluminum matrix and therefore surrounded by misfit dislocations as can be seen in Fig. 2. The orientation relationship between the G phase and the aluminum matrix has been reported [3] as $(310)_G \parallel (111)_{Al}$ and $(111)_G \parallel (310)_{Al}$ and our findings support it.

G" Phase - This phase was analyzed [3] as hexagonal with lattice parameter $a = 0.754$ nm, and $c/a = 1.04$. It is faulted parallel to the basal plane and thus its diffraction pattern contains streaks in the c direction. The plate normal of these particles is parallel to the c direction (Fig. 3). We have determined the orientation relationship between the G" phase and the aluminum matrix (Fig. 3) to be $(01\bar{1}3)_{G''} \parallel (111)_{Al}$, $[\bar{2}110]_{G''} \parallel [110]_{Al}$.

T Phase - This phase has the shape of an elongated plate, and was not completely

characterized. It has a complex faulted structure (Fig. 4) with the faults forming on planes perpendicular to its length, and it does not correspond to any previously reported phase. The crystallography of this phase and its orientation relationship with the matrix will be studied in the future.

The G' phase of Nes et al. [3], which was believed to be associated with impurities, was not detected in our samples.

On the x-ray diffractometer charts, peaks are seen corresponding to the Al_6Mn phase [11] and the G phase [2, 12, 13, 14, 15]: only peaks which correspond to reflections reported in the literature for these phases are seen. Table I presents a listing of the x-ray lattice parameter and precipitate phase results.

B. As-Spun Ribbons

The 3 wt.% Mn alloy is a supersaturated solid solution formed without microsegregation. Its microstructure consists of cell-free grains containing a high dislocation density (Fig. 5). At 5 wt.% Mn, two different runs on the melt spinner produced distinctly different ribbons; a thin, narrow ribbon and a thicker, wider ribbon which was produced when the nozzle of the melt spinner was moved closer to the wheel. Most of the ribbons at the other concentrations were intermediate in thickness between the two sets produced at 5 wt.% Mn. The thin (35 μm maximum thickness) and the thick (55 μm) ribbon of the 5 wt.% Mn alloy are distinctively different from one another. The microstructure of the thin ribbon is cell-free and resembles that of the Al-3 wt.% Mn alloy. The thick ribbon is cellular, with cell size about 2 μm , and contains unidentified precipitates at the cell boundaries and within the cells (Fig. 6). These two types of microstructure are probably related to differences in the solidification velocities of the ribbons.

The 9 wt.% Mn alloy has a cellular microstructure (Fig. 7) with average cell size of 1 μ m, and it contains fine precipitates at the cell boundaries. The alloys containing 12 and 15 wt.% Mn are both cellular in their as-spun condition. The cell boundaries contain fine precipitates but the cell interiors are mostly free from any precipitation (Figs. 8 and 9). The contrast difference between some of the cells indicates that these cell boundaries are also subgrain boundaries.

The small size of the cell boundary precipitates implies that these particles result from a solid state decomposition during cooling of the ribbon. The 15 wt.% Mn alloy contains regions with coarser precipitates, which could indicate a two-phase solidification process.

In the as-spun ribbons, only the aluminum phase is seen on the x-ray diffraction charts at compositions up to 12 wt.% Mn. Any other phases present are too small in volume to be detected. The lattice parameter (Fig. 10) decreases steadily with increasing Mn content. At 12 wt.% Mn the diffraction peaks of the as-spun ribbons are sharp but have a distinct tail on the low-angle side, indicative of a composition which is mostly uniform but contains local regions with a range of lower compositions. At 15 wt.% Mn, however, the as-spun ribbon shows two separate sets of Al peaks which correspond to material containing two different concentrations of Mn in solid solution. The peaks from the material containing the higher concentration of Mn are stronger relative to those from the less concentrated material on the side of the ribbon which was adjacent to the melt spinner wheel. In addition, the (111) and (222) reflections from the more concentrated material were especially intense, indicating a preferred orientation. Two weak peaks, attributed to precipitates, were also present but the phase could not be identified. Figure 10 shows lines representing previously reported results [1,16,17,18] for lattice parameters in rapidly quenched Al-Mn. Our own results are shown as solid points for samples in which

no cellular structure was observed by electron microscopy and as open circles for samples with cellular microstructures. The former group of points may be taken to represent the true concentration dependence of the lattice parameter, while the data from cellular samples are derived from lattices containing somewhat less than the nominal concentration of Mn in solid solution, with the remainder of the Mn being incorporated into micro-precipitates at the cell or grain boundaries. Note that the cell-free thin 5% Mn ribbon has a lattice parameter distinctly smaller than that of the thicker ribbon. This is consistent with the supposition that in the thicker ribbon the solidification rate was not great enough to incorporate all of the manganese into the supersaturated solid solution. Note also that the two lattice parameters observed in the 15 wt.% Mn sample indicate solid solution compositions of approximately 14 wt.% Mn and 3 wt.% Mn.

C. Heat Treated Ribbons

Following heat treatment at 450°C, subgrain boundaries are seen in all ribbons. In those ribbons which had a cellular solidification structure, the subboundaries in the annealed ribbons probably coincide with those which were present at the cell boundaries of the as-spun ribbons. In the ribbons which had no cellular solidification structure, subboundaries can be attributed to a polygonization process: in the case of the 3 wt.% Mn alloy these subboundaries were rather widely spaced compared to those which originate from solidification cells. In all ribbons, the distribution of the precipitating phases was found to be strongly correlated to the subgrain structure.

Up to 3 wt.% Mn

Following 1 hour at 450°C, TEM reveals that elongated Al₆Mn particles have precipitated along the subgrain boundaries of the Al-3 wt.% Mn. The subgrains contain a high density of dislocations (Fig. 11) and scattered events of precipitation can be observed in some of them.

A prolonged anneal of the 3 wt.% Mn alloy for 92 hours at 450°C results in three well defined types of precipitates. The first, globular in shape and up to 1 μm in diameter, was identified as G phase. The G phase particles have a high degree of coherence with the aluminum matrix as can be seen both in the diffraction pattern and by the presence of misfit dislocations at the semi-coherent boundary (Fig. 12). The second phase, consisting of elongated particles up to 2 μm in length, was identified as G" phase. The G" phase is faulted and the planar faults are perpendicular to the axis of its hexagonal structure, as indicated before [3]. The third phase was identified as Al_6Mn . The Al_6Mn particles are now not found on subgrain boundaries, probably due to grain boundary mobility in the annealing process.

X-ray measurements of the lattice parameter of the Al phase showed that in the ribbons containing 3 wt.% Mn or less, the supersaturation disappeared very slowly (Fig. 13). In the 2 and 3 wt.% Mn alloys, Al_6Mn could be detected in the x-ray diffraction charts after 1 hour at 450°C, but the peaks from this phase were very weak and remained so after much longer anneals. Very weak G peaks first appeared after 48 hours in the 2 wt.% Mn alloy, whereas in the 3 wt.% Mn alloy, weak G phase peaks first appeared at 16 hours and became strong at 48 hours.

5 wt.% Mn

The thick and thin ribbons of the Al-5 wt.% Mn alloy were heat treated for periods of 1 to 87 hours at 450°C. The microstructure of the ribbons following 1 hour at this temperature is shown by TEM to contain Al_6Mn particles along subgrain boundaries and a dispersed population of fine T type platelets within the grains (Fig. 14) except in a depleted zone adjacent to the subgrain boundaries. The T platelets are typically 100 to 300 nm long and 10 to 20 nm thick. The microstructure of the thick ribbon is different from the thin one in two ways.

The Al_6Mn particles at its subgrain boundaries are more globular and the depleted zone is typically 0.3 to 1 μm thick compared to 0.1 to 0.3 μm in the thin ribbons. These differences diminish after longer annealing times.

Specimens of both the thick and the thin ribbons that were heat treated for 3 hours at 450°C show some precipitate coarsening but are qualitatively identical to the ones heat treated for one hour. Following annealing for 16 hours, more coarsening is observed (Fig. 15) and after 48 hours or 65 hours the depleted zone comprises about 50% of the volume of the ribbon (Fig. 16). A comparison between the microstructures developed after 1 hour and 65 hours at 450°C (Figs. 14 and 16) reveals the following: The T phase particles are metastable at this temperature but they do not seem to be a precursor to the Al_6Mn . The Al_6Mn particles grow and become globular in time, and most of them are found on subgrain boundaries, with only a small proportion found within the grains. We tend to attribute the latter to subgrain migration rather than to a possible phase transformation between the T phase and the Al_6Mn .

X-ray diffraction reveals that the supersaturation was essentially gone after 1 hour (Fig. 13) for both the thin and thick ribbons. The long-time development of the diffraction peaks from the precipitate phases was dramatically different in the two cases. After one hour, both ribbons showed only Al_6Mn , and in the thin ribbon only this precipitate is seen even after the longest anneals (87 hours). In the thick ribbon, contrastingly, the G phase appears after 3 hours and steadily gains in strength until at 48 hours it is very strong and the Al_6Mn has decreased to a very weak level.

It is apparent from the results that the T phase precipitates either yield an x-ray diffraction pattern not clearly distinguishable from that of the G phase, or that they are too small to be detected by x-ray diffraction while the G phase particles are confined to parts of the ribbon not observed by TEM. Possible reasons that the two methods of analysis yield different readings of the relative abundance of the phases present will be considered in the discussion section.

9 wt.% Mn

Several heat treated ribbons of the 9 wt.% Mn alloy were studied by TEM. After 5 minutes at 450°C two phases are observed in the aluminum matrix (Fig. 17). One phase forms on subgrain boundaries, and is surrounded by a depleted zone. It is globular in shape with size averaging 0.5 μm in diameter. The second phase forms within the grain. These particles are needle-like in shape and measure up to 0.5 μm in length and 10 nm in thickness. Neither phase could be identified. Following a heat treatment of 1 hour, Al_6Mn particles are seen within the grains (Fig. 18) while most of the needle like phase disappears. After 16 hours at 450°C the Al_6Mn particles within the grains are about 0.5 μm long and large particles of G phase outline the subgrain boundaries (Fig. 19). The x-ray diffraction patterns showed Al_6Mn after only 5 minutes, but the G phase was first seen after a 16 hour heat treatment. The lattice parameter measurements reveal the rapid disappearance of the supersaturation during annealing of the 9 wt.% Mn alloy at 450°C, as shown in Fig. 20.

12 wt.% Mn

Following 1 hour at 450°C, Al_6Mn particles averaging 0.25 μm in length

are formed in the aluminum matrix (Fig. 21). These particles coarsen to about 0.5 μm following 3 hours at this temperature. A longer exposure of 22 hours results in the microstructure shown in Fig 22. The phases were identified as follows: an aluminum phase containing Al_6Mn particles and a G phase which contains a low density of aluminum particles.

The Al_6Mn x-ray diffraction peaks are strong after a 1 hour heat treatment, and a trace of the G phase is first seen at 3 hours. After 48 hours, the G phase peaks are very strong and the Al_6Mn peaks have diminished slightly.

15 wt.% Mn

Following 6 hours at 450°C the microstructure of the ribbon consists of three phases. Aluminum grains which contain Al_6Mn particles are shown in Fig. 23a. These particles are about 1 μm in size and their volume fraction is about 50%. Other grains are G phase and they contain Al_6Mn and aluminum particles, the size of which is about 300nm (Fig. 23b). The volume fraction of the particles is smaller in the G grains than in the aluminum grains. The x-ray diffraction pattern also shows Al, G, and Al_6Mn .

IV. DISCUSSION

Melt-spun ribbons are a convenient form of rapidly solidified material for transmission electron microscopy, because they can be thinned for examination without any previous cutting or sectioning operations: they are also convenient for x-ray diffraction. The TEM reveals the microstructural features including the identity of the phases and their distribution, while the x-ray diffraction reveals the lattice parameters and the relative overall abundance of the phases.

In some cases the two methods gave different indications of the occurrence and abundance of the phases, and several factors could explain this apparent discrepancy. Precipitate phases will yield measurable x-ray diffraction peaks only if they constitute at least a few percent of the sample, whereas TEM can detect the presence of minute or widely-scattered particles. Thus the x-rays failed to detect the micro-precipitates at the cell boundaries of as-spun ribbons, or the early stages of precipitation within the cells. However, the x-ray diffraction revealed a large difference between the thin and thick 5 wt.% Mn ribbons with respect to the relative abundance of the precipitate phases after long anneals, whereas TEM indicated a much smaller difference. This may be a result of selective observations by TEM, in that the thick 5 wt.% Mn ribbon was quite irregular in thickness and the TEM observations were necessarily confined to the thinnest parts of the ribbon.

At compositions up to 5 wt.% Mn, the as-spun ribbons showed no microsegregation and the lattice parameter indicated that all of the manganese was incorporated into the solid solution. At compositions greater than 5 wt.% Mn, or in thicker 5 wt.% Mn ribbons, a cellular or subgrain structure was present in the as-spun ribbons. Very small (<10nm diameter) precipitates were present along the cell or subgrain boundaries, and the concentration of Mn in solid solution within the cells was slightly less than the nominal composition of the sample. At 12 wt.% Mn the samples contained localized regions near the cell walls with dissolved manganese concentration less than that within the cell interiors. At 15 wt.% Mn, the ribbons contained both a solid solution containing close to the nominal concentration of Mn and other Al phase material with a much lower concentration of Mn, plus a significant volume fraction of a second phase.

Upon annealing at 450°C, precipitates grow rapidly along the subgrain

boundaries. It is not clear if the very small precipitates present at cell boundaries in the as-spun ribbons are the direct precursors of the rapidly growing precipitates. When more than about 4 wt.% Mn is in solid solution, precipitates also form within the subgrains but a denuded zone occurs adjacent to the boundaries.

We conclude that the subgrain boundaries, when present, acted as a high diffusivity network by means of which manganese moved to produce a rapid coarsening of precipitate particles lying along these boundaries. In ribbons containing a cellular solidification structure this process has already started during the cooling of the ribbons after melt spinning, as is shown by the presence in the as-spun ribbons of the fine precipitates along the cell boundaries.

Hood and Schultz [19] measured a diffusion coefficient of about 10^{-13} cm²/s for Mn in Al at 450°C and saw no difference in the rates for single crystal and polycrystal samples. They therefore concluded that diffusion along grain boundaries was not playing an important role. Buckle [20] earlier reported that the diffusion coefficient of Mn in Al decreases rapidly with increasing Mn content. Hood and Schultz found no such effect when they compared the diffusion rate in a sample doped with 0.25% Mn to the rates in very dilute samples. However, since the manganese-doped sample was a single crystal, its composition was much less than those of our samples, and the diffusion rate measurements on it were carried out at temperatures of 579°C or higher, the possibility of concentration-dependent or grain-boundary enhanced diffusion in our samples is not ruled out by the measurements of Hood and Schultz.

The G phase, if it ever nucleates on grain or cell boundaries in the less concentrated alloys, either does not grow sufficiently rapidly to attain detectable size before the supersaturation in these regions becomes depleted, or it dissolves in favor of Al₆Mn. Because the G phase is less stable than Al₆Mn at high

temperatures, G precipitates are less likely to have formed on the cell boundaries during the cooling after melt spinning. At higher concentrations, however, the locations of the Al_6Mn and G precipitates are interchanged.

In alloys which have neither a cellular structure nor a Mn concentration high enough to cause precipitation within the lattice, the supersaturation can persist for many hours. For alloys containing 5 wt.% Mn or more, the supersaturation disappears much more rapidly under the combined effects of rapid diffusion to precipitates along grain or cell boundaries and copious nucleation of one or more phases within the cells. The Al_6Mn , because of its more rapid growth, shows first in the x-ray diffraction, but the G phase becomes evident only after several hours of coarsening.

The G phase is generally regarded as being metastable with respect to Al_6Mn , but for our samples annealed at 450°C the G phase appeared in the x-ray diffraction patterns to be gaining in intensity while Al_6Mn decreased in intensity even at the longest times studied (up to 92 hours in the 3 wt.% Mn sample). Part of this intensity gain may be attributable to the coarsening of the G precipitates, which only after many hours become large enough to produce a strong diffracted intensity. However, our measurements as well as those of other investigators [2, 21] indicate that if the G phase is not stable at 450°C it is very close to being so. Bulk samples containing 3 to 9 wt.% Mn, which had been hot rolled at 600°C and subsequently annealed for 50-100 hours at 450°C, never showed any G phase. This can be attributed to the lack of sufficient supersaturation in these samples to ever nucleate the G phase. The G" and T phases were observed only in the 3 wt.% Mn and 5 wt.% Mn alloys, respectively. They never occurred in large volume fractions and at least the latter was metastable.

V. CONCLUSION

Several precipitate phases form in supersaturated Al-Mn solid solutions prepared by rapid solidification. At 450°C the G phase appears to be slightly more stable at long times than the Al₆Mn and the G" phase. Another phase, designated T, was detected in the Al-5 wt.% Mn ribbon, but it disappears during annealing. Cellular and subgrain structures, if present, play an important role in the precipitation process, and slight variations in the rapid solidification conditions, as in the 5 wt.% Mn ribbons, can determine which phase predominates after long anneals.

ACKNOWLEDGEMENTS

The authors thank DARPA for financial support of this work, and R. Mehrabian for useful discussions.

Figure Captions

- Fig. 1. Al_6Mn particles. The diffraction pattern represents a $[101]$ zone axis.
- Fig. 2. G phase particles. The diffraction pattern represents a $[001]$ zone axis.
- Fig. 3. G'' phase particle. The diffraction pattern represents a $[110]$ Aluminum zone axis and $(\bar{2}110)$ G'' zone axis.
- Fig. 4. T phase particles. Note faults perpendicular to its length and the resulting complex diffraction pattern.
- Fig. 5. As spun ribbon of Al-3 wt.% Mn alloy. The microstructure shows complete solubility of the manganese.
- Fig. 6. As spun thick ribbon of Al-5 wt.% alloy. Particles are seen at cell boundaries and within the cells.
- Fig. 7. As spun ribbon of Al-9 wt.% Mn alloy. A cellular microstructure with particles at the cell boundaries is observed.
- Fig. 8. As spun ribbon of Al-12 wt.% Mn alloy. A cellular microstructure with particles at the cell boundaries is observed.
- Fig. 9. As spun ribbon of Al-15 wt.% Mn alloy. Note the contrast difference between cells indicating that the cells are also subgrains.
- Fig. 10. X-ray lattice parameter of as spun Al-Mn ribbons compared to results of Falkenhagen et al. [1], Bhat et al. [18], Fridlyander et al. [16] and Yakunin et al. [17].
- Fig. 11. Al_6Mn particles at subgrain boundary of Al-3 wt.% Mn alloy annealed 1 hour at $450^\circ C$.
- Fig. 12. Misfit dislocations at the G phase-aluminum phase boundary (dark field, weak beam).
- Fig. 13. Lattice parameter of Al-Mn ribbons at different annealing times (x-ray diffraction measurements).
- Fig. 14. The Al-5 wt.% Mn alloy following 1 hour at $450^\circ C$, containing Al_6Mn particles along subgrain boundaries and T phase platelets within the grains.
- Fig. 15. Coarsening of the T phase in Al-5 wt.% Mn annealed for 16 hours at $450^\circ C$.
- Fig. 16. Al-5 wt.% Mn alloy following annealing for 65 hours at $450^\circ C$. T phase particles are found only in the center of the subgrains, and the depleted zone has grown.

- Fig. 18. Al_6Mn particles in the Al-9 wt.% Mn following 1 hour at 450°C .
- Fig. 19. The Al-9 wt.% Mn alloy following 16 hours at 450°C containing Al_6Mn particles within the grains and almost continuous G phase at subgrain boundaries.
- Fig. 20. X-ray lattice parameter measurements of Al-9 wt.% Mn as a function of annealing time.
- Fig. 21. Coarse Al_6Mn particles in Al-12 wt.% Mn following 1 hour at 450°C .
- Fig. 22. The microstructure of Al-12 wt.% Mn following 22 hours at 450°C containing three phases: Al_6Mn particles in aluminum grains and aluminum particles in the G grains.
- Fig. 23. The microstructure of Al-15 wt.% Mn following 6 hours at 450°C
(a) Al_6Mn particles in aluminum matrix.
(b) Al_6Mn and aluminum particles are found in G grains.

References

1. G. Falkenhagen and W. Hofmann, Z. Metal. 43, 69 (1952).
2. K. Little, G. V. Raynor, and W. Hume-Rothery, J. Inst. Met. 73, 83 (1946).
3. E. Nes, S. E. Naess, and R. Hoier, Z. Metal. 63, 248 (1972).
4. W. W. Mullins and R. F. Sekerka, J. Appl. Phys. 35, 444 (1964).
5. P. Furrer and H. Warlimont, Z Metall. 62, 100 (1971).
6. T. R. Anantharaman, P. Chandrarao, C. Suryanarayana, S. Lele and L. Chattopadhyay, Trans. Ind. Inst. of Metals 30, 423 and 434 (1977).
7. H. Jones, Aluminium 54, 274 (1978).
8. W. J. Boettinger, D. Shechtman, R. J. Schaefer, and F. S. Biancaniello, Met. Trans. 15A, 55 (1984).
9. R. J. Schaefer, S. R. Coriell, R. Mehrabian, C. Fenimore and F. S. Biancaniello, in Rapidly Solidified Amorphous and Crystalline Alloys, B. H. Kear, B. C. Giessen, and M. Cohen, eds., North Holland, New York, p. 79, 1982.
10. J. Narayan, J. Appl. Phys. 52, 1289 (1981).
11. A. D. I. Nicol, Acta Cryst. 6, 285 (1953).
12. K. Little and W. Hume-Rothery, J. Inst. Met. 74, 521 (1948).
13. G. Marchand, J. Inst. Met. 73, 747 (1947).
14. O. Izumi, D. Oelschlagel, and A. Nagata, Trans. Japan Inst. Met. 9, 227 (1968).
15. J. Adam and J. B. Rich, Acta Cryst. 7, 813 (1954).
16. I. N. Fridlyander, V. A. Konstantinov, and N. I. Zaitseva, Zhurnal Fizicheskoi Khimii, 30 (7), 1623 (1956).
17. A. A. Yakunin, I. I. Osipov, V. I. Tkach, and A. B. Lysenko, Fiz. Metal. Metalloved 43, 140 (1977).
18. S. P. Bhat, T. R. Ramachandran, and A. K. Jena, J. Mat. Sci. 9, 1759 (1974).
19. G. M. Hood and R. J. Schultz, Phil. Mag. 23, 1479 (1971).
20. H. Buckle, Z. Electrochem. 49, 238 (1943).
21. K. Kusumoto and M. Ohta, Journ. Inst. Poltechn. Osaka Univ. 5 (6), 57 (1954); Nippon Kinzoku Gakki-Si, 18 (8),

TABLE I. SUMMARY OF X-RAY DIFFRACTION RESULTS

Wt.% Mn	Time at 450°C (hrs.)	Lattice Parameter a(nm)	Al ₆ Mn Intensity*	G Intensity*
0.1	0	0.40492	0	0
	3	0.40495	0	0
1.0	0	0.40460	0	0
	1	0.40475	0	0
	16	0.40475	0	T
2.0	0	0.40424	0	0
	1	0.40440	VW	0
	3	0.40452	0	0
	16	0.40467	VW	0
	48	0.40487	VW	VW
3.0	0	0.40392	0	0
	1	0.40392	VW	0
	1	0.40409	W	0
	3	0.40423	T	0
	3	0.40406	VW	0
	16	0.40485	VW	W
	48		VW	S
	92	0.40488	VW	S
5.0 (thin)	0	0.40301	0	0
	1	0.40496	VW	0
	3	0.40502	W	0
	16	0.40493	M	0
	48		M	0
	65		M	0
	87		W	0
5.0 (thick)	0	0.40352		
	1	0.40494	M	0
	3	0.40499	W	M
	16	0.40504	M	S
	48		VW	VS
9.0	0	0.40238	0	0
	0.08	0.40311	VW	0
	0.17	0.40459	M	0
	0.33	0.40477	M	0
	1	0.40500	M	0
	3	0.40501	S	0
	16	0.40511	M	W

Table I (cont.)

Wt.% Mn	Time at 450°C (hrs.)	Lattice Parameter a(nm)	Al ₆ Mn Intensity*	G Intensity*
12.0	0	0.40157	0	0
	0	0.40157	0	0
	0	0.40157	0	0
	0	0.40174	0	0
	1	0.40512	S	0
	3	0.40523	S	T
	16	0.40537	S	S
	22		M	VS
	48		M	VS
15.0	0	3.9994		
		4.0371		
	1		W	S
	6		W	VS

*Intensities: 0 = not detected, T = trace, VW = very weak, W = weak, M = medium, S = strong, VS = very strong.

Fig 1



Fig 2



Fig 3



Fig 4

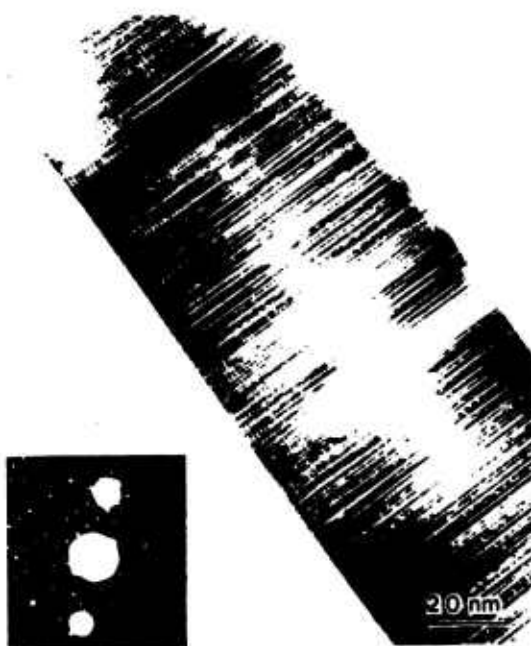


Fig 5



Fig 6



Fig 7



Fig 8



Fig 9



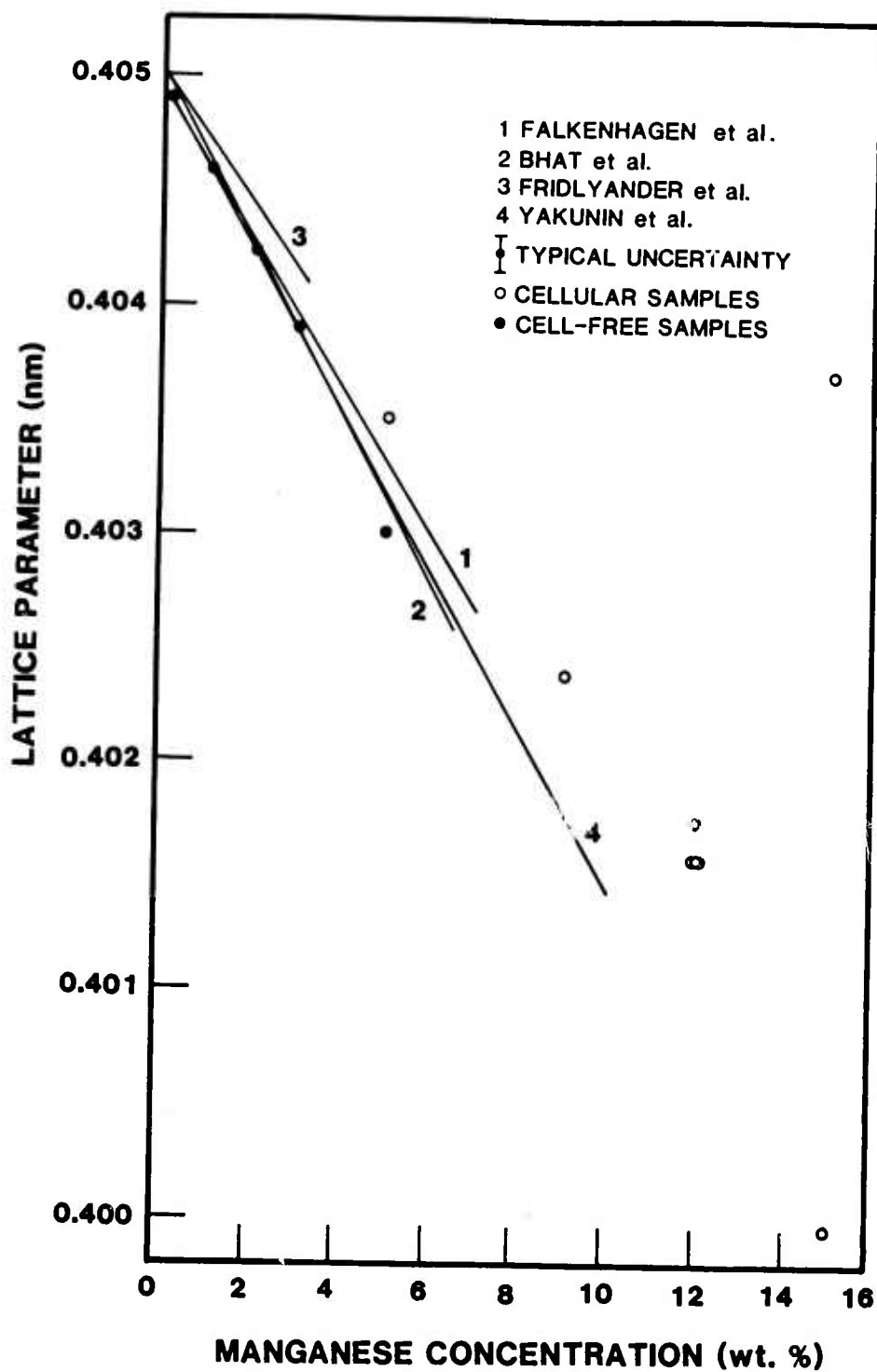


Fig. 11



Fig. 12



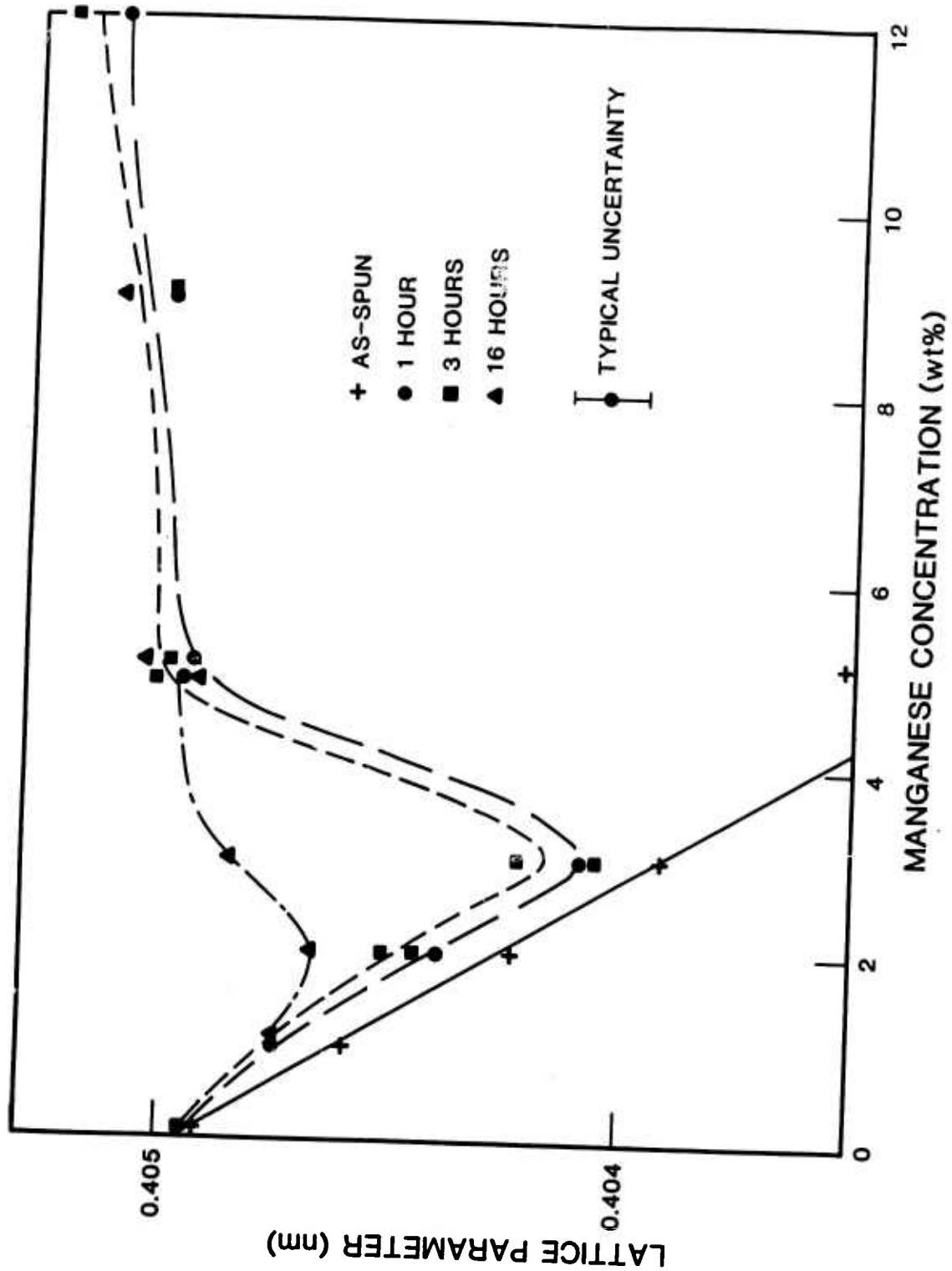


Fig 14



Fig 15



Fig 16



Fig 17



Fig 18



Fig 19



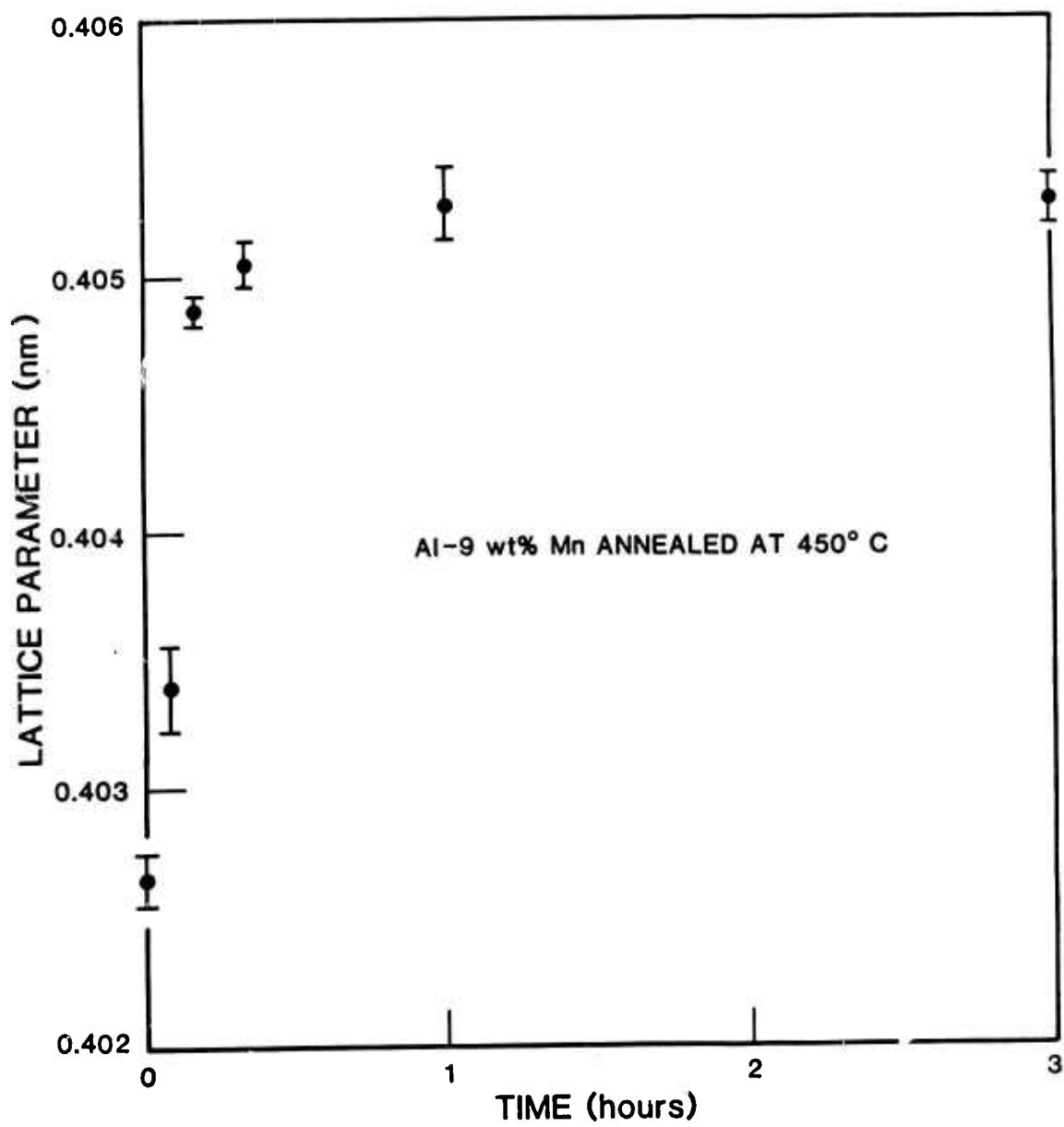




Fig 21



Fig 22



Fig 23 a



Fig 23 b